

Omnisoot: an object oriented package for process design of gas phase synthesis of Carbon black

Mohammad Adib^{1,*}, Sina Kazemi¹, M. Reza Kholghy^{1,*}

Abstract

A computational tool, omnisoot, was developed utilizing the chemical kinetics capabilities of Cantera to model the formation of carbonaceous nanoparticles, such as soot and carbon black (CB), from the reactions of gaseous hydrocarbons. Omnisoot integrates constant volume, constant pressure, perfectly stirred, and plug flow reactor models with four inception models from the literature, as well as two particles dynamics models: a monodisperse (MPBM) and a sectional population balance models (SPBM). This package serves as an integrated process design tool to predict soot mass, morphology, and composition under varying process conditions. The modeling approach accounts for soot inception, surface growth, and oxidation, coupled with detailed gas-phase chemistry, to close the mass and energy balances of the gas-particle system; subsequently, soot and gas-phase chemistry are linked to the particle dynamics models that consider the evolving fractal-like structure of soot agglomerates. The developed tool was employed to highlight the similarities and differences among the implemented inception models in predicting soot mass, morphology, and size distribution for three use-cases: methane pyrolysis in a shock tube, ethylene pyrolysis in a flow reactor, and ethylene combustion in a perfectly stirred reactor. The simulations of 5% CH₄ pyrolysis in shock-tube with short residence times (≈ 1.5 ms) demonstrated that multiple combinations of inception and surface growth rates minimized the prediction error for carbon yield but led to markedly different morphologies, emphasizing the need for measured data on soot morphology to constrain inception and surface growth rates. The comparison of simulation results in a pyrolysis flow reactor at three different flow rates suggested that only irreversible models can predict bimodality in particle size distribution. Moreover, the contributions of inception and surface growth to the total soot mass were used as determining factors in soot morphology.

¹Department of Mechanical and Aerospace Engineering, Carleton University, 1125 Colonel By Dr, Ottawa, ON K1S 5B6, Canada

*Correspondeing author

List of potential journals

- Chemical Engineering Journal
- Combustion and Flame
- Powder Technology

List of potential reviewers

- Dr. José Moran, Assistant professor at University of Ottawa, jose.moran@uottawa.ca
- Dr. Seth Dworkin, Professor at Toronto Metropolitan University, seth.dworkin@torontomu.ca
- Dr. Chiara Saggese, Researcher at Lawrence Livermore National Laboratory, saggese1@llnl.gov

Nomenclature

Acronyms

CFD	Computational Fluid Dynamics
DEM	Discrete Element Modelling
HACA	Hydrogen abstraction carbon addition
MPBM	Monodisperse Population Balance Model
SPBM	Sectional Population Balance Model

Constants

A_v	Avogadro's number	$6.02214076 \times 10^{23}$	1/mol
k_B	Boltzmann constant	$1.3806488 \times 10^{-23}$	J/K

English symbols

C_{tot}	Total carbon content of soot particles (per section)	mol/kg
D	Diffusion coefficient of particles	m^2/s
d	Diameter	m
d_c	Collision diameter	m
d_g	Gyration diameter	m
D_H	Duct hydraulic diameter	—
d_m	Mobility diameter	m
d_p	Primary particle diameter	m
$E(m)$	Absorption function of soot	—
f	Friction factor	—
h	Enthalpy	J/kg
H_{tot}	Total hydrogen content of soot particles (per section)	mol/kg
I	Source terms for soot variables	$\text{mol}/(\text{kg} \cdot \text{s})$
k	Reaction rate constant	$\text{m}^3/(\text{mol} \cdot \text{s})$
Kn	Knudsen number	—
m	Mass	kg
n_p	Number of primary particles of per agglomerate	—
N_{agg}	Number density of agglomerates	mol/kg
N_{pri}	Number density of primary particles	mol/kg
R_H	Duct hydraulic radius	—
SF	Sectional spacing factor	—
T	Temperature	K
u	Internal energy	J/kg
W	Molecular weight	kg/mol

Greek symbols

β	Collision frequency	m^3/s
δ_a	Mean distance of particles	m
λ	Mean free path	m
λ_a	Mean stopping distance of particles	m
ν	Gas kinematic viscosity	m^2/s
ρ	Density	kg/m^3
φ	Soot volume fraction based on reactor volume	kg/m^3
f_v	Soot volume fraction based on gas volume	m^3/m^3

Subscripts

ads	Adsorption
-----	------------

agg	Agglomerate
coag	Coagulation
cont	Continuum
f	Forward
fm	Free molecular
g	Gyration
grow	Surface growth
inc	Inception
m	Mobility
ox	Oxidation
pri	Primary particle
r	Reverse
reac	Reactive

1 Introduction

The formation of carbonaceous nanoparticles such as soot and Carbon Black (CB) is a complex and multi-scale process that involves chemical reactions, heat transfer, fluid and particle dynamics and spans over wide ($\sim 10^{-12}$ to 1 m) and time ($\sim 10^{-15}$ to 1 s) scales. Figure 1 demonstrates the length and time scales relevant to different stages of soot formation from PAH precursors to incipient, nascent, and mature soot in flames. Understanding the effect of process parameters on particle concentration, morphology, and composition is not trivial, but crucial due to health and environmental impacts of soot and functional properties of CB.

Soot is a broad-band light absorber [1], and is emitted on a large scale (~ 9.5 megatons per year [2]) acting as the third strongest contributor to climate change after methane and carbon dioxide. Its fine particulate nature (PM_{2.5}) also raises health concerns [3]. In contrast, CB, the largest flame-made nanomaterial by production volume (~ 15 megatons annually [4]), plays a critical role in industrial applications, including rubber reinforcement [5] and lithium-ion batteries [6].

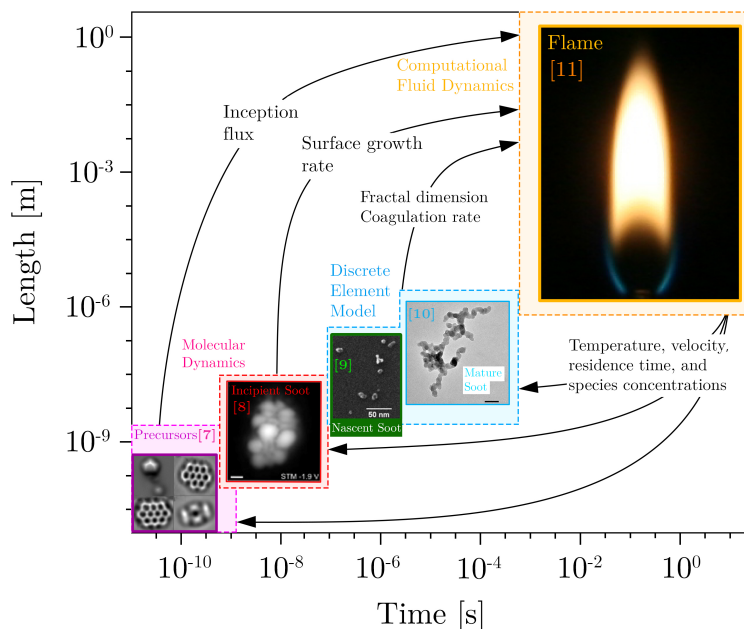


Figure 1: The time and length scales of the processes involved in soot formation span a wide range including molecular reactions between precursors, surface growth and coagulation of incipient and nascent soot particles, and their maturity that depends on the temperature-time history determined by the flame velocity and temperature.

Controlling CB yield, structure, morphology, and composition is essential for producing specific grades tailored to various applications in both conventional (e.g., furnace process [12]) and emerging production methods [13, 14, 15]. However, the influence of process parameters such as feedstock composition, pressure, and temperature-time history on CB properties remains incompletely understood due to the complexities of gas-phase chemistry and the intricate nature of CB formation (as discussed in the following sections). This highlights the need for robust computational models to predict yield, particle structure, and composition under different process conditions and to mitigate soot emissions from combustion systems.

"Soot" and "Carbon Black" are distinct materials in terms of chemical properties and synthesis processes [16]. While, soot usually refers to unwanted particulate matter formed during incomplete combustion with variable organic content and a large variation in carbon to hydrogen (C/H) ra-

tio [16], CB is commercially produced under highly controlled partial combustion or thermal decomposition of hydrocarbons. However, soot particles generated under controlled laboratory conditions can have similar structure and composition to CB. Mature soot formed in methane and ethylene premixed flames can reach elemental C/H \approx 20 [17], which is close to C/H of CB. The comparison of Transmission Electron Microscopy (TEM) images of industrially produced CB [18] with soot sampled from diesel fuel [19, 20] indicates similarities in their morphology and structure. Hereafter, soot will be used to collectively refer to carbonaceous nanoparticles produced during combustion/pyrolysis processes.

Soot inception is believed to begin with the formation of Polycyclic Aromatic Hydrocarbons (PAHs) in the gas phase and followed by their transition into incipient particles. Soot inception, remains poorly understood at the level of pathways and elementary reactions [21]. This lack of understanding stems primarily from uncertainties in PAH chemistry and the kinetics of PAH growth into soot particles, a process that is highly reversible and thus sensitive to local conditions such as temperature, pressure, and the concentrations of intermediate species [21].

The classic description of soot inception relies on PAH dimerization where collision of two PAH molecules (monomers in this context) forms a dimer held together by van der Waals forces (vdW) [22]. The dimerization is an irreversible process with an efficiency that accounts for the reversibility or dissociation of dimers. The theory postulates that PAH growth continues by sequential addition of monomers forming stacks of dimers, trimers, tetramers, and so on to reach a certain mass threshold that marks the emergence of incipient soot [22], but for practical purposes, a dimer is usually considered as incipient soot. Here, we call this model *Irreversible Dimerization*. Irreversible Dimerization has been used to predict soot formation in burner-stabilized premixed [23, 24], counterflow diffusion flames [25, 26], coflow diffusion flames [27, 28], etc. A collision efficiency factor ranging between 10^{-6} to 1 is also employed to adjust the inception flux and PAH adsorption rates to achieve desired soot mass and size distribution. PAHs of moderate sizes, such as pyrene (4 rings) to coronene (7 rings), have been considered as the starting point of inception due to their thermodynamic instability, which justifies the irreversibility at high temperatures [22]. However, the theoretical calculations [29] and experiments [30] indicate that PAH dimerization is highly reversible in flame conditions. The inception flux of irreversible dimerization is mainly controlled by PAH concentration due to its weak temperature dependence, so it produces new particles at low temperatures (even below 500 K) [31] despite experimental evidence for termination of inception below 1200 K [32, 33].

Kholghy et al. [34] emphasized the necessity of chemical bond formation after physical PAH clustering for accurate prediction of volume fraction, primary particle diameter and Particle Size Distribution (PSD) in ethylene coflow diffusion flames. Later, Kholghy et al. [35] proposed the *"Reactive Dimerization"* model which starts with reversible collision of PAHs leading to physical dimers held with vdW forces that are graphitized and form chemically-bonded dimers that serve as incipient soot that grows via coagulation and surface reactions. They also performed a systematic analysis of the contribution of different PAHs, and concluded that one- and two-ring aromatics account for almost all of inception flux in the so-called *"sooting flame"* [24]. However, Frenklach and Mebel [36] pointed out that an inception model that initiates with a highly reversible step similar to Reactive Dimerization [35] cannot produce sufficient flux of particles to match measurements of the benchmark burner-stabilized stagnation flame [37]. Instead, they proposed the H-abstraction-C₂H₂/Carbon-addition mechanism [22, 38] (HACA)-driven mechanism where addition of a monomer molecule to its radical activated by hydrogen abstraction forms a stable dimer via an E-Bridge bond formation, and this sequential process continues to form trimers, tetramers, and larger PAH clusters. Blanquart and Pitsch [39] proposed a two-step irreversible inception model where self collision of PAHs with specified efficiencies results in the formation of dimers that collide and subsequently coalesce into an incipient soot.

The gas-phase chemistry of aromatics can be extended to account for chemical growth of incipient soot via surface reactions [40]. This hypothesis, known as "chemical similarity", postulates that the reactions occurring on the soot surface are similar to those involving large molecules of PAHs in the gas phase. It also provides a means to describe the rates of surface growth and particle oxidation in terms of elementary chemical reactions. In other words, it is assumed that the surface of soot particles is made up of lateral faces of large PAHs covered with C-H bonds. This is the basis

for HACA mechanism [22, 38] that assumes the soot surface consists of hydrogenated sites with a predefined density. Mass growth on the soot surface requires H-abstraction to form a radical site, followed by acetylene attack similar to the growth of PAH molecules in the gas phase. The reactivity of these sites changes with time and temperature [41, 42], described as soot aging. For modelling purposes, a temperature-dependent surface reactivity, usually represented by α , was introduced to account for the effect of temperature-time history. Appel et al. [38] showed α changes with temperature and particle size in laminar premixed flames.

Adsorption of PAHs on the surface of soot particles is also a viable growth mechanism [22], more specifically called physisorption or chemisorption depending on the mechanisms driving the adsorption process [43]. There is still debate over the stability of adsorbed PAH molecules on soot surface [44]. Following the hypothesis that PAHs are building blocks of soot particles, a mechanism similar to inception is often used to describe PAH-soot growth.

In typical soot formation processes, such as those occurring in flames and reactors, inception and surface growth are active for only a relatively short duration compared to the total residence time of soot particles. Subsequently, due to high particle concentrations, coagulation becomes the dominant mechanism, rapidly leading to the development of both a Self-Preserving Size Distribution (SPSD) [45] and an asymptotic fractal-like structure [46, 47]. The collision frequency of agglomerates depends on their evolving fractal-like morphology, with polydisperse agglomerates colliding more frequently than monodisperse ones. This enhancement reaches an asymptotic value of 35% [47] in the free molecular regime or 82% [48] in the transition regime at SPSPD, irrespective of primary particle polydispersity.

Particle morphology, governed by inception, surface growth, and agglomeration, can be precisely tracked using mesoscale simulations such as Discrete Element Modeling (DEM) [49] provided that the gas-to-particle mass flux through inception and surface growth is known a priori. However, these methods are computationally expensive, and integrating them with chemical kinetics in Computational Fluid Dynamics (CFD) frameworks is challenging [50]. Consequently, their application is often limited to canonical scenarios where particle dynamics are solved independently of chemistry and flow dynamics—for instance, by populating the simulation domain with incipient particles, thereby bypassing the inception step, and neglecting gas removal or addition associated with soot formation [51] as it is difficult to have a particle dynamics modeled fully coupled with gas chemistry.

As a computationally efficient alternative, particle dynamics can be tracked by Eulerian approaches such as the Method of Moments (MOM) [52] or Monodisperse Population Balance Models (MPBM) [53]. Such models only track average particle properties (e.g., moment ratios) and their accuracy can be limited if unrealistic assumptions (e.g., approximating agglomerates as monodisperse and perfect spheres) are used. However, when inception and surface growth are short [54] and high particle number concentrations are formed [51], they lead to rapid attainment of SPSPD and agglomerates having asymptotic structure [47]. In this case, a MPBM or MOM can be assembled on a firm scientific basis with accuracy on par with DEM [49] and experimental data [55, 56, 57]. Such models can be readily interfaced with CFD simulations [58] without significant computational cost, making them ideal for three-dimensional and even turbulent flame simulations.

The MOM tracks moments of the PSD and estimates average particle properties such as mass [59], surface area [39], the number of constituent primary particles per agglomerate, n_p [52], or even particle composition [60] using the ratio of the moments. The MOM with interpolative closure (MOMIC) was developed to predict simultaneous inception, surface growth and coagulation of soot agglomerates and estimates its PSD with six equations [52]. To calculate source terms of the transported moments, additional moments that are not tracked are needed, preventing the closure of the system of differential equations with the MOM [59, 61]. Thus, often the PSD shape is assumed a priori [59] or extra equations are solved to estimate it [53]. In contrast, MPBMs do not have the closure problem and calculate average particle properties by tracking their total concentration, mass [53] and area [62, 63].

Sectional Population Balance Models (SPBMs), similar to MPBMs but capable of tracking agglomerate and primary PSDs [64], are widely used in complex laminar [27] and turbulent flows [65]. SPBMs can solve one, two, or three equations per section, with their capabilities depending on the number of equations solved: single-equation models track basic properties like total mass or number

concentration [66], two-equation models capture additional details such as surface area or primary particle number [67], and three-equation models enable detailed tracking of complex properties like composition or morphology [27]. Coupled with relations for fractal-like structure [68] and collision frequency [69], SPBMs accurately model particle size distribution, morphology, and composition. However, their computational cost rises exponentially with the number of sections [70] and tracked properties [27]. SPBMs are gaining attention, due to the recent increase in computational resources, for simulating laminar and turbulent benchmark flames in two-dimensional domains, even with moderately large chemical mechanisms. For example, the CoFlame solver [71], designed to simulate laminar diffusion flames in axisymmetric domains using sn SPBM, has been employed in numerous studies, demonstrating its ability to accurately capture soot morphological properties [72, 73]. Kholghy et al. extended the SPBM in CoFlame to predict soot maturity by analyzing the equilibrium nanostructure of PAHs within soot primary particles, distinguishing nascent from mature soot based on an isotropic core-graphitic shell structure and surface PAH configuration [27]. More recent developments have further refined SPBMs by incorporating the persistent radical nature of soot particles, improving the description of inception, surface growth, and oxidation in laminar premixed and counterflow flames [74]. This approach employs a sectional method in which soot particles are tracked using discrete size bins (BINs), allowing detailed resolution of the size distribution and chemical composition. The algorithm systematically groups PAHs, primary particles, and aggregates into BINs based on carbon atom count and H/C ratio, capturing the evolution of particle size and morphology. By treating large PAHs and soot aggregates as resonantly stabilized radicals, the model reduces the reliance on explicit H-abstraction reactions and improves agreement with experimental data for several ethylene laminar premixed flames and counterflow diffusion at different pressures, maximum flame temperatures and soot yields. However, the implementation relies on a customized chemical mechanism, which imposes constraints on modifying individual soot evolution processes, such as inception, growth, or oxidation, without adapting the entire framework [75, 76].

Here, we develop a computational package, called *omnisoot*, which integrates Cantera [77] as a chemistry solver to simulate soot formation in reduced-order dimensions. The package provides a versatile soot model that can be coupled with all reaction mechanisms. Both particle dynamics models (MPBM and SPBM) are coupled with various soot inception and surface growth models, offering flexibility to study soot formation alongside gas phase chemistry. This package facilitates fundamental investigations of soot formation, including pathway analysis, reaction mechanism evaluation, and inception flux estimation, while also supporting process design and optimization of CB production in industrial reactors under diverse fuel compositions, temperatures, pressures, and residence times. The theoretical background and governing equations for sub-models of *omnisoot* are detailed in subsequent sections, followed by validation against benchmark DEM simulations and verification of mass and energy conservation across all models. Finally, three use cases—shock tubes, flow reactors, and perfectly stirred reactors—demonstrate the capability of *omnisoot* to predict gas chemistry, soot yield, structure, and size distribution.

2 Theoretical Foundation & Governing Equations

The mathematical basis for *omnisoot* is explained in the top-to-bottom hierarchical order. First, the governing equations for constant volume, constant pressure, perfectly stirred and plug flow reactor models are reviewed in Sections 2.2.1-2.2.4. These equations differ from pure gas-phase transport formulation as they consider the solid phase. The transport equations of “soot variables” include source terms that accounts for change in each soot variable due to inception, surface growth, oxidation and coagulation. Then, particle dynamics models are explained in Sections 2.3 that entails description of size distribution and morphology of soot particles and their collision rate, which is used to determine the coagulation source term. Section 2.5 focuses on the “*PAH growth model*”s that take care of inception and adsorption from designated precursors and calculates the corresponding source terms. Similarly, the “*surface reactions*” model are detailed in Section 2.4 that elaborates on the surface growth and oxidation rates based on HACA mechanism. Finally, the rate of addition or removal of gaseous species due to soot formation is explained in Section S1. Figure 2 illustrates the

general structure of omnisoot and the sub-models.

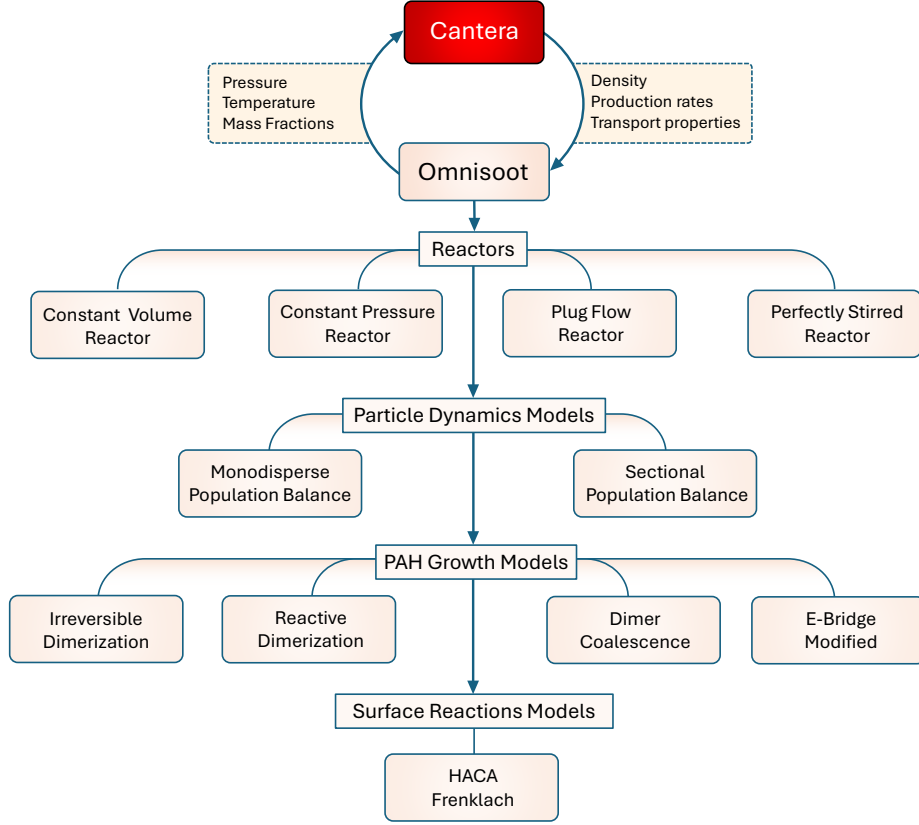


Figure 2: The structure of omnisoot that illustrates the coupling with Cantera and submodels including reactors, particle dynamic models, PAH growth models and surface reactions models

2.1 Assumptions and conventions

Here, the main conventions and assumptions used in the derivation of the mathematical model are listed below.

1. The ideal gas law is used to calculate physical, transport, and chemical properties of gas mixture.
2. f_v and φ denote the volume of soot particles normalized by the gas volume and reactor volume, respectively. Their relationship can be expressed as:

$$\begin{aligned}
 f_v &= \frac{V_{soot}}{V_{gas}} \\
 \varphi &= \frac{V_{soot}}{V_{gas} + V_{soot}} \\
 \varphi &= \frac{f_v}{1 + f_v}.
 \end{aligned} \tag{1}$$

3. \dot{s}_k denotes the rate production/consumption of k_{th} gaseous species due to soot inception, surface growth and oxidation. It is positive when the species is released to gas mixture.

4. Each soot agglomerate consist of monodisperse spherical primary particles, which are in point contact. So, the model does not consider formation of necking (or sintering) in soot agglomerates by surface growth.
5. The primary particles of each agglomerate are similar enough that can be described by mean size and composition.
6. The word “*particle*” refers to soot both in spherical and agglomerate shape.
7. The density of soot is assumed constant at the value of 1800 kg/m³. Soot density changes with its maturity level, which is often linked to the elemental C/H ratio of soot particles [78]. Here, the considered value represents an average between density of mature soot with high C/H ratios ($\rho = 2000\text{kg/m}^3$) and that of nascent soot with low C/H ratios ($\rho = 1600\text{kg/m}^3$) [79, 78].
8. The incipient soot particles are 2 nm in diameter, so the model does not allow particles with a primary particle diameter smaller than 2 nm. The number of carbon atoms in the incipient soot particle ($n_{c,min}$) is calculated from the mass of a sphere with the diameter of 2 nm ($d_{p,min}$) assuming pure carbon content.

$$d_{p,min} = 2 \text{ nm}$$

$$n_{c,min} = \frac{\pi}{6} \rho_{soot} d_{p,min}^3 \frac{1}{W_{carbon}} \approx 378. \quad (2)$$

9. The calculation of PAH adsorption and soot oxidation requires “*soot concentration*” which is defined as the number of soot agglomerates per unit volume of gas. The number density of agglomerates, N_{agg} , are tracked per unit mass of gas mixture i.e. *mol/kg_{gas}*. So, soot concentration can be calculated by multiplying agglomerate number density by gas density as:

$$[\text{soot}] = \rho \cdot N_{agg}. \quad (3)$$

10. The specific heat, internal energy and enthalpy of soot are approximated by those of pure graphite, and employed to close the energy balance in the system [80].
11. Soot particles and gas are in thermal equilibrium during soot formation processes, and there is no temperature gradient within each agglomerate.
12. ψ denotes a *soot variable* that represents a mean property of soot particles (or a section) tracked in omnisoot by solving transport equations including total concentration of agglomerates, N_{agg} and primary particles, N_{pri} , and total carbon, C_{tot} and hydrogen content, H_{tot} of soot. S_ψ is the source term of the soot variable, ψ that appears in soot equations.
13. *PAH growth* is a sub-model of omnisoot with a set of pathways that determine the rate of inception and adsorption from PAHs (designated as soot precursors) in the gas mixture.
14. *Surface reactions* is a sub-model of omnisoot that describes the addition of acetylene to soot surface, and removal of carbon via oxidation by OH and O₂ following the HACA scheme. The model does not consider soot oxidation with CO₂, H₂O and NO_x.
15. The single superscript, i denotes the section number of a soot variable or a derived property. For example, d_p^i is the primary particle diameter of section i . The double superscript, ij represents a property related to two sections. For example, β^{ij} is the collision frequency of the sections i and j . In case of the monodisperse model, the section number can be ignored because it is equivalent to the sectional model with one section.
16. The computation of morphological parameters (d_p , d_m , d_g , and n_p) and diffusion coefficient are done similarly in both particle dynamics models, but they are explained separately in Section 2.3.1.

Table 1: The names, symbols, chemical formula and molecular weight of the soot precursors used by omnisoot

Species name	Symbol	Chemical formula	W [kg/mol]
Naphthalene	A2	C ₁₀ H ₈	0.128
Phenanthrene	A3	C ₁₄ H ₁₀	0.178
Pyrene	A4	C ₁₆ H ₁₀	0.202
Acenaphthylene	A2R5	C ₁₂ H ₈	0.152
Acephenanthrylene	A3R5	C ₁₆ H ₁₀	0.202
Cyclopentapyrene	A4R5	C ₁₈ H ₁₀	0.226

17. *precursors* refers to the PAHs larger than naphthalene used for inception and surface growth (PAH adsorption). The list of precursors with their chemical formula and molecular mass is provided in Table 1. It should be noted that the precursors can be dynamically changed by omnisoot’s user interface.

2.2 Reactors

The governing equations of reactor models implemented in omnisoot are briefly presented in the following sections. The control volume encompasses the gas mixture and soot particles, as illustrated in Figure 3. The equations ensure conservation of total mass and energy of the gas and particle system which can also receive or lose heat through the reactor walls.

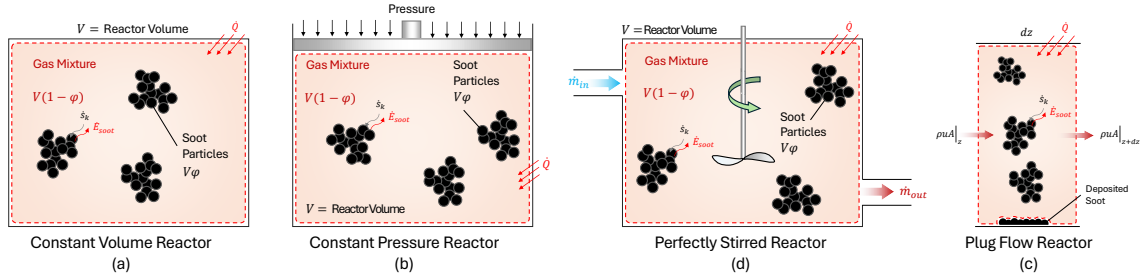


Figure 3: The schematics of constant volume reactor (a), constant pressure reactor (b) plug flow reactor (c), and perfectly stirred reactor (d)

2.2.1 Constant Volume Reactor (CVR)

In this reactor, the volume of gas mixture changes during the process but the reactor volume (the sum of volume of gas mixture and solid particles) stays constant.

The mass balance equation is written as:

$$\frac{d}{dt}(m) = (1 - \varphi)V \sum_i \dot{s}_i W_i, \quad (4)$$

where m is the mass of gas mixture. The rate of change of m is equal to the rate of production of soot mass. Similarly, the species equation for species k is expressed as:

$$\frac{dY_k}{dt} = \frac{1}{\rho} (\dot{\omega}_k + \dot{s}_k) W_k - \frac{1}{\rho} Y_k \sum_i \dot{s}_i W_i. \quad (5)$$

The transport equation for a generic soot variable, ψ can be written as:

$$\frac{d\psi}{dt} = S_\psi - \frac{\psi}{\rho} \sum_i \dot{s}_i W_i. \quad (6)$$

The energy balance for the gas mixture is written in terms of the rate of change of temperature. An external heat source of \dot{Q} is considered to account for possible heat loss/gain of the reactor.

$$\begin{aligned} \frac{dT}{dt} = \frac{1}{\rho c_v + \rho_{soot} f_v c_{soot}} & \left[- \sum_k e_k (\dot{\omega}_k + \dot{s}_k) W_k \right. \\ & \left. + e_{soot} \sum_k \dot{s}_k W_k + \frac{\dot{Q}}{V(1-\varphi)} \right]. \end{aligned} \quad (7)$$

where $\rho_{soot} f_v c_{soot}$, and $e_{soot} \sum_k \dot{s}_k W_k$ represents the formation and sensible energy of soot, respectively. We investigated the effect of considering soot formation and sensible energy on gas and soot properties by simulating the pyrolysis of 30%CH₄-Ar with and without considering the above mentioned term. As shown in Figure S1a, neglecting soot sensible energy results in the overprediction of temperature by nearly 150 K and mobility diameter by a factor of 3 during the 80 ms of the simulation. The overprediction of temperature changes gas chemistry leading to a noticeable decrease in the residual methane and benzene (Figure S1b).

2.2.2 Constant Pressure Reactor (CPR)

CPR is a closed system similar to CVR, but the pressure stays constant throughout the process, which means the boundaries of the system can move changing its volume.

The rate change of mass, species, and soot variables for the CPR are the same as CVR given in Equations (4), (5), and (6), respectively. The energy equation is written as:

$$\begin{aligned} \frac{dT}{dt} = \frac{1}{\rho c_p + \rho_{soot} f_v c_{soot}} & \left[- \sum_k h_k (\dot{\omega}_k + \dot{s}_k) W_k \right. \\ & \left. + h_{soot} \sum_k \dot{s}_k W_k + \frac{\dot{Q}}{V(1-\varphi)} \right]. \end{aligned} \quad (8)$$

2.2.3 Perfectly Stirred Reactor (PSR)

In this reactor, gas enters with a mass flow rate \dot{m}_{in} , composition of Y_{in} and temperature of T_{in} , instantaneously mixes and homogeneously reacts with the mixture resident inside the reactor. The reacting gas reaches a spatially uniform temperature and composition described by T , and Y . It is assumed that temperature, composition and soot properties of the outflow are the same as the mixture inside reactor. As shown in Figure 3d, \dot{m}_{in} and \dot{m}_{out} refer to inflow and outflow gas mass flow rates, respectively. Under no-soot conditions, the inlet and outlet mass flow rates are equal, but the gas mixture loses mass by soot formation, so \dot{m}_{out} is slightly less than \dot{m}_{in} . The pressure of reactor is assumed to stay constant during the process [81]. The nominal residence time of gas mixture in the reactor is defined as:

$$\tau = \frac{\rho V}{\dot{m}_{in}}. \quad (9)$$

The conservation of mass can be written for PSR by considering the mass flux of in- and outflow, and the removal of mass due to soot generation as:

$$\frac{dm}{dt} = \dot{m}_{in} - \dot{m}_{out} + V(1-\varphi) \sum_i \dot{s}_i W_i. \quad (10)$$

Gas composition is obtained by solving the species transport equations as:

$$\frac{dY_k}{dt} = \frac{\dot{m}_{in}}{\rho V (1 - \varphi)} (Y_{k,in} - Y_k) + \frac{1}{\rho} \left[(\dot{\omega}_k + \dot{s}_k) W_k - Y_k \sum_i \dot{s}_i W_i \right]. \quad (11)$$

The soot transport equations can also be expressed as:

$$\frac{d\psi}{dt} = \frac{\dot{m}_{in}}{\rho V (1 - \varphi)} (\psi_{in} - \psi) + S_\psi - \frac{1}{\rho} \psi \sum_i \dot{s}_i W_i. \quad (12)$$

The energy equation for this reactor is written as:

$$\begin{aligned} \frac{dT}{dt} = \frac{1}{\rho c_p + \rho_{soot} c_{p,soot} f_v} & \left[\frac{\dot{m}_{in}}{V(1 - \varphi)} (h_{in} - h) - \frac{\dot{m}_{in}}{V(1 - \varphi)} \sum_k (Y_{k,in} - Y_k) h_k \right. \\ & \left. - \sum_k (\dot{\omega}_k + \dot{s}_k) W_k h_k + \sum_i \dot{s}_i W_i h_{soot} + \frac{\dot{Q}}{V(1 - \varphi)} \right]. \end{aligned} \quad (13)$$

2.2.4 Plug Flow Reactor (PFR)

PFR is an ideal representation of a channel or duct with a steady-state one-dimensional flow changes temperature, composition, and soot properties along the channel. There is no spatial gradient over the cross-section due to strong mixing, and diffusion along the channel is negligible.

The continuity equation for PFR is written as:

$$\frac{d\dot{m}}{dz} = (1 - \varphi) A \sum_i \dot{s}_i W_i. \quad (14)$$

The momentum equation can also be established as:

$$u(1 - f_v) \sum_i \dot{s}_i W_i + \rho u(1 - \varphi) \frac{du}{dz} = -\frac{d}{dz} (p(1 - \varphi)) - \frac{\tau_w}{R_H}, \quad (15)$$

where τ_w is the wall shear the can be determined from friction factor, f , as:

$$\tau_w = \frac{1}{2} \rho u^2 f, \quad (16)$$

where f can be calculated with a good accuracy for the entire range of Reynolds number, Re , from laminar to turbulent flow using the explicit formula given by Haaland [82]:

$$\frac{1}{f^{1/2}} = -1.8 \log \left(\frac{6.9}{Re} + \left[\frac{\epsilon/D_H}{3.7} \right]^{1.11} \right), \quad (17)$$

where ϵ is the roughness of reactor wall. R_H and D_H are hydraulic radius and diameter, respectively that can be determined from cross-section geometry of reactor as:

$$D_H = 4R_H = \frac{4A_c}{P_c}, \quad (18)$$

where A_c and P_c are cross-sectional area and wetted perimeter of the reactor. The species equation can be expressed as:

$$\frac{dY_k}{dz} = \frac{1}{\rho u} \left[(\dot{\omega}_k + \dot{s}_k) W_k - Y_k \sum_i \dot{s}_i W_i \right]. \quad (19)$$

The soot transport equations can also be written as:

$$\frac{d\psi}{dz} = \frac{S_\psi}{u} - \frac{\psi}{\rho u} \sum_i \dot{s}_i W_i - \frac{4}{D_H} \frac{k_{dep}^i \psi}{u}, \quad (20)$$

where k_{dep}^i is the deposition velocity of soot particles of section i calculated as:

$$k_{dep} = \frac{Sh \cdot D^i}{D_H}, \quad (21)$$

where Sh is the Sherwood number, which is 3.66 for a laminar flow and calculated using the Berger and Hau correlation [83] for the turbulent flow in terms of Re and Sc , Schmidt number as:

$$Sh = 0.0165 Re^{0.86} Sc^{1/3}. \quad (22)$$

The energy equation can be expressed as:

$$\frac{dT}{dz} = \frac{1}{\rho u c_p + \rho_{soot} u f_v c_{p,soot}} \left[- \sum_k h_k (\dot{\omega}_k + \dot{s}_k) W_k + h_{soot} \sum_k \dot{s}_k W_k + q'' \frac{P_c}{A} \right] \quad (23)$$

where q'' is the wall heat flux provided as a function of reactor length or flow residence time that represents external heating or heat loss in the reactor.

2.3 Particle Dynamics Model

Population balance models rely on the Eulerian description of particles where bulk properties of particle population such as number density, mass or surface area are treated as continuous quantities and tracked by solving scalar transport equations. These methods are computationally cheaper compared with mesoscale models such as DEM, and can be easily interfaced with chemical kinetics in CFD solvers to simulate soot formation in laminar and turbulent configurations. Here, we use two particle dynamics models: a monodisperse population balance model (MPBM) based on four variables leading to 4 transport equations in total, and a fixed sectional population balance model (SPBM) tracking three variables per section. The total number of transport equations in the sectional model is determined by the number of sections and number of equations solved per section. The first two/three variables in the MPBM/SPBM enables description of number, mass, and evolving fractal-like morphology of soot agglomerates that are necessary to accurately predict collision frequency of agglomerates [84] as well as oxidation and surface growth rates [85]. The last variable tracks the number of hydrogen atoms in agglomerates that allows the model to capture the soot composition, thereby its maturity [27], and surface reactivity [60].

The tracked variables are used to address particle dynamics that includes (i) determining particles morphology and composition from tracked soot variables, (ii) calculating collision frequency and coagulation source term, (iii) computing the source terms that appear in soot transport equations of the reactors (Equations(6), (12) and (20)). by from the contribution of inception, PAH adsorption, surface growth and oxidation. First, we review the common features of both particle dynamics models: morphology, diffusion, coagulation frequency and composition of soot particles. Then, the particular characteristics of the MPBM and SPBM are explained that entails (i) calculating the coagulation rate of section(s) (ii) combining the contribution of inception, surface growth, oxidation, and coagulation to source term of soot variables. As mentioned before, any parameter with superscript i denotes the section number, which can be ignored for the MPBM that only has one section. For example, d_m^i can be replaced with d_m .

2.3.1 Soot Morphology

The evolving fractal-like structure of agglomerates is quantified by their mobility diameter normalized by primary particle diameter, d_m/d_p , and gyration diameter, d_m/d_g , that can be described with power-laws derived from mesoscale simulations. Incipient soot is initially a sphere formed of PAHs with constant density that grows in size by surface reactions and forms agglomerates by coagulation.

The collision frequency of particles depends on their evolving fractal-like structure [84]. Mobility and gyration diameters are calculated using power-laws developed to describe the morphology of soot from premixed [55], diffusion [86] flames, and diesel engines [87]. Figure 4 illustrates the schematics of a soot agglomerates with 12 primary particles and depicted d_p , d_m , and d_g .

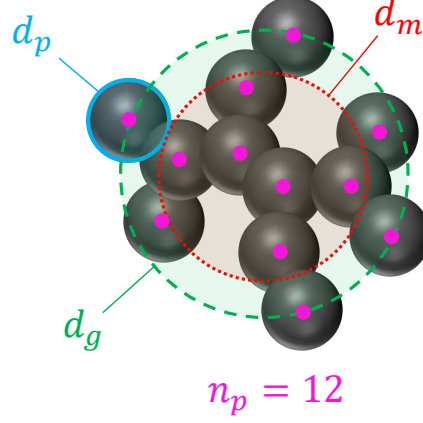


Figure 4: The schematics of a soot agglomerates with 12 primary particles ($n_p = 12$). Primary particle, d_p , mobility d_m , and gyration d_g , diameters are shown.

n_p^i is the number of primary particles per agglomerate of i^{th} section that can be obtained by dividing the number concentration of primary particles in i^{th} section by that of agglomerates in that section as:

$$n_p^i = \frac{N_{pri}^i}{N_{agg}^i}. \quad (24)$$

Primary particle diameter, d_p^i , can be obtained from total carbon content and number density of primary particles using

$$d_p^i = \left(\frac{6}{\pi} \frac{C_{tot}^i \cdot W_{carbon}}{\rho_{soot}} \frac{1}{N_{pri}^i \cdot Av} \right)^{1/3}. \quad (25)$$

The DEM-derived power-laws [51] relate d_m^i and d_g^i to d_p^i and n_p^i as

$$d_m^i = d_p^i \cdot n_p^{i 0.45}, \quad (26)$$

$$d_g^i = \begin{cases} d_m^i / (n_p^{i -0.2} + 0.4), & \text{if } n_p^i > 1.5 \\ d_m^i / 1.29, & \text{if } n_p^i \leq 1.5 \end{cases} \quad (27)$$

The collision diameter, d_c^i , is the maximum of d_m^i and d_g^i :

$$d_c^i = \max(d_m^i, d_g^i), \quad (28)$$

where d_m^i , d_g^i , and d_c^i are used to calculate the source terms of the surface growth, oxidation, PAH adsorption and coagulation. The volume equivalent diameter, d_v^i , is the diameter of the sphere with the same mass as agglomerate, and it is obtained as:

$$d_v^i = d_p^i \cdot n_p^{i 1/3}. \quad (29)$$

The primary particle surface area is calculated from d_p^i assuming spherical primary particles.

$$A_p^i = \pi d_p^{i 2}, \quad (30)$$

A_{tot}^i (for each section) is defined as the total surface area of soot particles per unit mass of gas mixture obtained as

$$A_{tot}^i = N_{pri}^i \cdot Av \cdot A_p^i. \quad (31)$$

2.3.2 Diffusion of soot particles

The diffusion coefficient of soot particle, D^i , is calculated as

$$D^i = \frac{k_B T}{f^i}, \quad (32)$$

where f^i is the friction factor of particles in gas and calculated as

$$f^i = \frac{3\pi\mu d_m^i}{C^i(d_m^i)}, \quad (33)$$

where C^i is the Cunningham function, which applies a correction to the particle friction factor in the continuum regime to account for non-continuum effects in the transition and free molecular regimes, as:

$$C^i(d) = 1 + \frac{2\lambda}{d} \left(1.21 + 0.4 \cdot \exp\left(\frac{-0.78d}{\lambda}\right) \right), \quad (34)$$

where λ is the mean free path of gas given as:

$$\lambda = \frac{\mu}{\rho} \sqrt{\frac{\pi W_{gas}}{2k_B AvT}}. \quad (35)$$

Note that, λ is a property of the gas mixture that does not depend on particle morphology and size section. The mean velocity, c^i , and mean stop distance of particles, λ_a^i , can be calculated as:

$$c^i = \sqrt{\frac{8k_B T}{\pi m_{agg}^i}}. \quad (36)$$

$$\lambda_a = \frac{8D^i}{\pi c^i}. \quad (37)$$

The mean distance of particles is also calculated as:

$$\delta_a^i = \frac{1}{d_c^i \lambda_a^i} \left[(d_c^i + \lambda_a^i)^3 - (d_c^i{}^2 + \lambda_a^i{}^2)^{3/2} \right] - d_{c,j}. \quad (38)$$

2.3.3 Coagulation efficiency of soot particles

The coagulation efficiency of soot particles is commonly assumed as unity meaning that every collision between two soot particles successfully results in formation of a new agglomerate. However, numerical models [88] and experimental evidence [89] showed that the coagulation efficiency drastically decrease for particles smaller than 10 nm in the free molecular regime ($Kn \gg 10$) due to their high kinetic energy that exceeds the attractive forces [90]. The coagulation efficiency of two colliding particles can be described as [88]:

$$\zeta^{ij} = 1 - \left(1 + \frac{\Phi_0^{ij}}{k_B T} \right) \exp \left(-\frac{\Phi_0^{ij}}{k_B T} \right), \quad (39)$$

where Φ_0 is the potential well depth i.e. the minimum interaction energy between two colliding particles. Hou et al. [91] calculated Φ_0 for soot particles 1-15 nm by considering the attraction and repulsion between constituent carbon and hydrogen atoms, and proposed an equation based on the reduced diameter, d_r^{jk} , of colliding particles as:

$$\Phi_0^{ij} = -6.6891 \times 10^{-23} (d_r^{jk})^3 + 1.244 \times 10^{-21} (d_r^{jk})^2 + 1.1394 \times 10^{-20} d_r^{jk} - 5.5373 \times 10^{-21} \quad (40)$$

$$d_r^{jk} = \frac{d_c^i \cdot d_c^j}{d_c^i + d_c^j} \quad (41)$$

Equation (40) is valid for d_r^{jk} between 1 and 7 nm, and ζ^{ij} is assumed as unity for particles with reduced diameter larger than 7 nm.

2.3.4 Soot Composition

The composition of soot characterized by their elemental carbon to hydrogen ratio (C/H) is a measure of soot maturity and increases from $C/H < 2$ for incipient soot [92] to $2 < C/H < 10$ for nascent soot [93] and $C/H > 20$ for mature soot [94]. The soot agglomerates are assumed to have pure carbon graphitic core [27] with all hydrogen atoms on the surface [60]. C/H ratio can be obtained from total carbon and hydrogen content as:

$$\left(\frac{C}{H}\right)^i = \frac{C_{tot}^i}{H_{tot}^i}. \quad (42)$$

The carbon content of each agglomerate is a predefined parameter in the SPBM (depending on the section the agglomerate is placed), but it can be calculated from dividing C_{tot} by N_{agg} for the MPBM. The hydrogen content of each agglomerate is calculated for both particle dynamics models as:

$$H_{agg}^i = \frac{H_{tot}^i}{N_{agg}^i}. \quad (43)$$

2.3.5 Monodisperse Population Balance Model

The MPBM used in this research tracks the number density of primary particles, N_{pri} , and agglomerates, N_{agg} , total carbon, C_{tot} , and hydrogen, H_{tot} , content of soot particles per unit mass of gas mixture. The morphological parameters such as primary particle, mobility and gyration diameters obtained from these soot variables are the average values for the population.

2.3.5.1 Coagulation

Coagulation is the process during which solid and hard soot particles collide and attach at point of contact leading to larger agglomerates. This process conserves the soot mass and composition and number density of primary particles, so coagulation only affects N_{agg} . I_{coag} accounts for the decay rate of N_{agg} by the binary collision of soot particles by

$$I_{coag} = -\frac{1}{2} \zeta \beta N_{agg}^2, \quad (44)$$

where β is the collision frequency of agglomerates for the free molecular ($Kn > 10$) to continuum regime ($Kn < 0.1$), and ζ is the coagulation efficiency calculated by Equation (39). The value of β in the transition regime ($0.1 < Kn < 10$) can be calculated from the harmonic mean of the continuum (β_{cont}) and free molecular (β_{fm}) regime values. Additionally, an enhancement factor of 1.82 is applied to take into account the effect of polydispersity [48] in the monodisperse as:

$$\beta = 1.82 \frac{\beta_{fm} \beta_{cont}}{\beta_{fm} + \beta_{cont}}, \quad (45)$$

$$\beta_{fm} = 4\sqrt{\frac{\pi k_b T}{m_{agg}}} d_c^2, \quad (46)$$

$$\beta_{cont} = 8\pi d_c D. \quad (47)$$

Alternatively, β can be obtained using Fuchs interpolation [95] as:

$$\beta = \beta_{cont} \left(\frac{d_c}{d_c + 2\sqrt{2}\delta} + \frac{8D}{\sqrt{2}c_r d_c} \right)^{-1}. \quad (48)$$

2.3.5.2 Source terms

The source terms of tracked variables combines the effect of the inception, PAH adsorption, surface growth and oxidation and coagulation.

$$S_{N_{agg}} = \frac{I_{N,inc}}{n_{c,min}} + I_{coag}. \quad (49)$$

$$S_{N_{pri}} = \frac{I_{N,inc}}{n_{c,min}}. \quad (50)$$

$$S_{C_{tot}} = I_{C_{tot},inc} + I_{C_{tot},gr} + I_{C_{tot},ads} + I_{C_{tot},ox}. \quad (51)$$

$$S_{H_{tot}} = I_{H_{tot},inc} + I_{H_{tot},gr} + I_{H_{tot},ads} + I_{H_{tot},ox}. \quad (52)$$

The partial source terms in Equations 49-52 denoted by I are determined by surface reaction and PAH growth models explained in Sections 2.4 and 2.5 respectively.

2.3.6 Sectional Population Balance Model

A SPBM with the fixed pivot employing the fixed pivot technique is utilized to describe particle dynamics [96]. The particle mass range is divided into discrete sections, each representing agglomerates of identical mass. Inception introduces new particles to the first section with the mass corresponding to the incipient particle (≈ 378 carbon atoms). Particles in the first section can migrate to higher sections by gaining mass through surface growth and coagulation, or return to lower sections by losing mass via oxidation. Particle fragmentation is not considered. The mass of each section is determined using a geometric progression, with a scale factor equal to the mass of the incipient soot particle and a common ratio known as the sectional spacing factor, SF . By default, the number of sections and the spacing factor are set to 60 and 1.5, respectively; however, both parameters can be dynamically adjusted through the omnisoot user interface. The mass of each section is approximated by the carbon content (in moles) of agglomerates in moles as:

$$C_{agg}^i = \frac{n_{c,min}}{Av} \cdot SF^{(i-1)}, \quad (53)$$

where $(i - 1)$ represents the exponent of SF . The mass of hydrogen is neglected in the placement of agglomerates in the sections. The total number densities of agglomerates, N_{agg}^i , and primary particles, N_{pri}^i are tracked for each section. Morphological parameters are determined for each section according to the equations in Section 2.3.1.

2.3.6.1 Coagulation

In SPBM approach, collisions between particles from every two sections are considered. The new particles formed by coagulation are placed in an upper section with the mass equal to sum of mass of particles involved in the collision. When the mass of yielded particle lies between two consecutive sections, the particles are divided among these sections proportional to their mass. One possible scenario is that the mass of the newly formed particle is greater than the last section, thus leaving tracked mass range. Losing mass is a potential problem with the fixed pivot sectional model, which

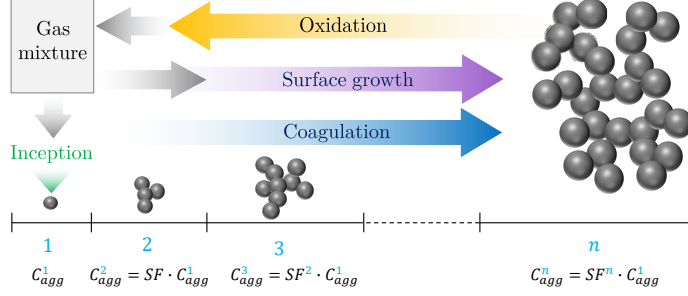


Figure 5: The illustration of sections of SPBM. The mass of sections grows progressively by the scale factor of SF . Inception introduces new particles to the first section that propagate to the upper section via coagulation and surface growth and return to lower sections by oxidation.

can be avoided by selecting proper number of sections and spacing factor to keep the number of agglomerates to a minimum in the last sections during the simulation.

The collision frequency between sections j and k can be obtained from the harmonic mean of the values in the continuum and free molecular regimes as:

$$\beta^{jk} = \frac{\beta_{fm}^{jk} \beta_{cont}^{jk}}{\beta_{fm}^{jk} + \beta_{cont}^{jk}}, \quad (54)$$

$$\beta_{fm}^{jk} = \sqrt{\frac{\pi k_b T}{2} \left(\frac{1}{m_{agg}^j} + \frac{1}{m_{agg}^k} \right) (d_c^j + d_c^k)^2}, \quad (55)$$

$$\beta_{cont}^{ij} = \frac{2k_B T}{3\mu} \left(\frac{C^j}{d_m^j} + \frac{C^k}{d_m^k} \right) (d_c^j + d_c^k)^2. \quad (56)$$

The collision frequency can also be determined from the Fuchs interpolation similar to the MPBM as:

$$\beta^{jk} = \beta_{cont}^{ij} \left[\frac{d_c^j + d_c^k}{d_c^j + d_c^k + 2 + \delta_r^{jk}} + \frac{8(D^j + D^k)}{\bar{c}_r^{jk} (d_c^j + d_c^k)} \right]^{-1}, \quad (57)$$

where δ_r^{jk} and \bar{c}_r^{jk} are the mean square root of mean distance and velocity of particles, respectively.

$$\delta_r^{jk} = \sqrt{\delta_a^{j2} + \delta_a^{k2}}, \quad (58)$$

$$\bar{c}_r^{jk} = \sqrt{c^{j2} + c^{k2}}. \quad (59)$$

Coagulation redistributes the total number of agglomerates and primary particles as well as hydrogen atoms among the sections. The partial coagulation source terms for N_{agg}^i , N_{pri}^i and H_{tot}^i can be calculated as:

$$I_{N_{agg}}^i = \sum_{k=1}^{n_{sec}} \sum_{j=k}^{n_{sec}} \left(1 - \frac{\delta_{jk}}{2} \right) \eta_{ijk} \zeta^{jk} \beta^{jk} N_{agg}^j N_{agg}^k - N_{agg}^i \sum_{k=1}^{n_{sec}} \zeta^{im} \beta^{im} N_{agg}^m. \quad (60)$$

$$I_{N_{pri}}^i = \sum_{k=1}^{n_{sec}} \sum_{j=k}^{n_{sec}} \left(1 - \frac{\delta_{jk}}{2} \right) \eta_{p,ijk} \eta_{ijk} \zeta^{jk} \beta^{jk} N_{agg}^j N_{agg}^k - N_{pri}^i \sum_{k=1}^{n_{sec}} \zeta^{im} \beta^{im} N_{agg}^m. \quad (61)$$

$$I_{H_{tot}}^i = \sum_{k=1}^{n_{sec}} \sum_{j=k}^{n_{sec}} \left(1 - \frac{\delta_{jk}}{2} \right) \eta_{h,ijk} \eta_{ijk} \zeta^{jk} \beta^{jk} N_{agg}^j N_{agg}^k - H_{tot}^i \sum_{k=1}^{n_{sec}} \zeta^{im} \beta^{im} N_{agg}^m. \quad (62)$$

where δ_{jk} is the Kronecker delta defined as:

$$\delta_{jk} = \begin{cases} 1, & \text{if } j = k \\ 0, & \text{if } j \neq k \end{cases} \quad (63)$$

In Equation (60), η_{ijk} assigns newly formed agglomerates to the two consecutive sections in order to conserve mass during coagulation [97].

$$\eta_{ijk} = \begin{cases} \frac{C_{agg}^{i+1} - C_{agg}^{jk}}{C_{agg}^{i+1} + C_{agg}^i}, & \text{if } C_{agg}^i \leq C_{agg}^{jk} < C_{agg}^{i+1} \\ \frac{C_{agg}^i - C_{agg}^{jk}}{C_{agg}^i + C_{agg}^{i-1}}, & \text{if } C_{agg}^{i-1} \leq C_{agg}^{jk} < C_{agg}^i \\ 0 & \text{else} \end{cases}, \quad (64)$$

where $C_{agg}^{jk} = C_{agg}^j + C_{agg}^k$. Similarly, $\eta_{p,ijk}$ in Equation (61) and $\eta_{h,ijk}$ in Equation (62) adjust the number primary particles and hydrogen atoms added to consecutive sections based on their mass, respectively.

$$\eta_{p,ijk} = \frac{C_{agg}^i}{C_{agg}^{jk}} (n_p^j + n_p^k), \quad (65)$$

$$\eta_{h,ijk} = \frac{C_{agg}^i}{C_{agg}^{jk}} (H_{agg}^j + H_{agg}^k), \quad (66)$$

2.3.6.2 Source terms

The source terms are split into four parts showing the contribution of different soot formation and evolution factors. The effect of surface growth and PAH adsorption are combined because they are similar mass-gaining mechanisms.

$$S_{N_{agg}} = (S_{N_{agg}})_{inc} + (S_{N_{agg}})_{gr,ads} + (S_{N_{agg}})_{ox} + (S_{N_{agg}})_{coag}, \quad (67)$$

$$S_{N_{pri}} = (S_{N_{pri}})_{inc} + (S_{N_{pri}})_{gr,ads} + (S_{N_{pri}})_{ox} + (S_{N_{pri}})_{coag}, \quad (68)$$

$$S_{H_{tot}} = (S_{H_{tot}})_{inc} + (S_{H_{tot}})_{gr,ads} + (S_{H_{tot}})_{ox} + (S_{H_{tot}})_{coag}. \quad (69)$$

Inception introduces equal number of agglomerates and primary particles to the first section.

$$(S_{N_{agg}})_{inc} = \frac{1}{Av} \frac{I_{N,inc}}{C_{agg}^i}, \quad (70)$$

$$(S_{N_{pri}})_{inc} = \frac{1}{Av} \frac{I_{N,inc}}{C_{agg}^i}, \quad (71)$$

$$(S_{H_{tot}})_{inc} = I_{H,inc}. \quad (72)$$

In Equations 70 and 71, $i = 1$ so C_{agg}^i . Surface growth and PAH adsorption increase the carbon and hydrogen content of agglomerates, and transfer them to upper sections. The removal rate of agglomerates (N_{agg}^i) from the original section due to surface growth and PAH adsorption must be equal to the addition rate of agglomerates to the target section to conserve the mass, and it is calculated by dividing the mass growth rate by the difference of the mass of the adjacent sections.

$$(S_{N_{agg}})_{gr,ads} = \frac{1}{Av} \begin{cases} -\frac{I_{C_{tot},gr}^i + I_{C_{tot},ads}^i}{C_{agg}^{i+1} - C_{agg}^i} & \text{if } i = 1 \\ \frac{I_{C_{tot},gr}^{i-1} + I_{C_{tot},ads}^{i-1}}{C_{agg}^i - C_{agg}^{i-1}} - \frac{I_{C_{tot},gr}^i + I_{C_{tot},ads}^i}{C_{agg}^{i+1} - C_{agg}^i} & \text{if } 1 < i < n_{sec} \\ \frac{I_{C_{tot},gr}^{i-1} + I_{C_{tot},ads}^{i-1}}{C_{agg}^i - C_{agg}^{i-1}} & \text{if } i = n_{sec} \end{cases} \quad (73)$$

As agglomerates move up/down through sections, they carry the number of primary particles as well as hydrogen atoms, so the transfer rate of agglomerates is multiplied by n_p^i and H_{agg}^i , respectively.

$$(S_{N_{pri}})_{gr,ads} = \frac{1}{Av} \begin{cases} -\frac{I_{C_{tot},gr}^i + I_{C_{tot},ads}^i}{C_{agg}^{i+1} - C_{agg}^i} & \text{if } i = 1 \\ \frac{I_{C_{tot},gr}^{i-1} + I_{C_{tot},ads}^{i-1}}{C_{agg}^i - C_{agg}^{i-1}} n_p^{i-1} - \frac{I_{C_{tot},gr}^i + I_{C_{tot},ads}^i}{C_{agg}^{i+1} - C_{agg}^i} n_p^i & \text{if } 1 < i < n_{sec} \\ \frac{I_{C_{tot},gr}^{i-1} + I_{C_{tot},ads}^{i-1}}{C_{agg}^i - C_{agg}^{i-1}} n_p^{i-1} & \text{if } i = n_{sec} \end{cases} \quad (74)$$

$$(S_{H_{tot}})_{gr,ads} = \frac{1}{Av} \begin{cases} -\frac{I_{C_{tot},gr}^i + I_{C_{tot},ads}^i}{C_{agg}^{i+1} - C_{agg}^i} H_{agg}^i + I_{H_{tot},gr}^i + I_{H_{tot},ads}^i & \text{if } i = 1 \\ \frac{I_{C_{tot},gr}^{i-1} + I_{C_{tot},ads}^{i-1}}{C_{agg}^i - C_{agg}^{i-1}} H_{agg}^{i-1} - \frac{I_{C_{tot},gr}^i + I_{C_{tot},ads}^i}{C_{agg}^{i+1} - C_{agg}^i} H_{agg}^i + I_{H_{tot},gr}^i + I_{H_{tot},ads}^i & \text{if } 1 < i < n_{sec} \\ \frac{I_{C_{tot},gr}^{i-1} + I_{C_{tot},ads}^{i-1}}{C_{agg}^i - C_{agg}^{i-1}} H_{agg}^{i-1} + I_{H_{tot},gr}^i + I_{H_{tot},ads}^i & \text{if } i = n_{sec} \end{cases} \quad (75)$$

Similarly, the agglomerates lose (carbon) mass by oxidation, and descend to the lower sections carrying primary particle and hydrogen.

$$(S_{N_{agg}})_{ox} = \frac{1}{Av} \begin{cases} \frac{I_{C_{tot},ox}^{i+1}}{C_{agg}^{i+1} - C_{agg}^i} - \frac{I_{C_{tot},ox}^i}{C_{agg}^i} & \text{if } i = 1 \\ \frac{I_{C_{tot},ox}^{i+1}}{C_{agg}^{i+1} - C_{agg}^i} - \frac{I_{C_{tot},ox}^i}{C_{agg}^i - C_{agg}^{i-1}} & \text{if } 1 < i < n_{sec} \\ -\frac{I_{C_{tot},ox}^i}{C_{agg}^i - C_{agg}^{i-1}} & \text{if } i = n_{sec} \end{cases} \quad (76)$$

$$(S_{N_{pri}})_{ox} = \frac{1}{Av} \begin{cases} \frac{I_{C_{tot},ox}^{i+1}}{C_{agg}^{i+1} - C_{agg}^i} n_p^{i+1} - \frac{I_{C_{tot},ox}^i}{C_{agg}^i} & \text{if } i = 1 \\ \frac{I_{C_{tot},ox}^{i+1}}{C_{agg}^{i+1} - C_{agg}^i} n_p^{i+1} - \frac{I_{C_{tot},ox}^i}{C_{agg}^i - C_{agg}^{i-1}} n_p^i & \text{if } 1 < i < n_{sec} \\ -\frac{I_{C_{tot},ox}^i}{C_{agg}^i - C_{agg}^{i-1}} n_p^i & \text{if } i = n_{sec} \end{cases} \quad (77)$$

$$(S_{H_{tot}})_{ox} = \frac{1}{Av} \begin{cases} \frac{I_{C_{tot},ox}^{i+1}}{C_{agg}^{i+1} - C_{agg}^i} H_{agg}^{i+1} - \frac{I_{C_{tot},ox}^i}{C_{agg}^i} H_{agg}^i + I_{H_{tot},ox}^i & \text{if } i = 1 \\ \frac{I_{C_{tot},ox}^{i+1}}{C_{agg}^{i+1} - C_{agg}^i} H_{agg}^{i+1} - \frac{I_{C_{tot},ox}^i}{C_{agg}^i - C_{agg}^{i-1}} H_{agg}^i + I_{H_{tot},ox}^i & \text{if } 1 < i < n_{sec} \\ - \frac{I_{C_{tot},ox}^i}{C_{agg}^i - C_{agg}^{i-1}} H_{agg}^i + I_{H_{tot},ox}^i & \text{if } i = n_{sec} \end{cases} \quad (78)$$

2.4 Surface Reactions model

The heterogeneous surface reactions are described by HACA. The soot growth in HACA scheme is based on a sequential process similar to PAH growth. The hydrogenated arm-chair sites ($C_{soot} - H$) on the edge of aromatic rings are dehydrogenated by H abstraction forming C_{soot}° that bonds with C_2H_2 resulting in an additional aromatic ring with hydrogenated site. These sites can also be attacked by O_2 or OH leading to removal of carbon from soot particles by oxidation. The elementary reactions that describe this sequential process are listed in Table 2. The rate of mass growth by HACA is obtained from the reaction of C_2H_2 with dehydrogenated sites as:

$$\omega_{gr}^i = \alpha^i k_{f4} [C_2H_2] [C_{soot}^\circ], \quad (79)$$

where k_{f4} denotes the forward rate of Reaction 2 in Table 2, and $[C_{soot}^\circ]$ is obtained by multiplying the surface density of dehydrogenated sites, χ_{soot}° with total surface area of soot (per unit of mass of gas mixture) as:

$$[C_{soot}^\circ] = \frac{\rho}{Av} A_{tot}^i \cdot \chi_{soot}^\circ, \quad (80)$$

where χ_{soot}° is calculated by assuming the steady-state for $[C_{soot}^\circ]$ in the system of reactions in Table 2.

$$\chi_{soot}^\circ = \frac{k_{f1}[H] + k_{f2}[OH]}{k_{r1}[H_2] + k_{r2}[H_2O] + k_{f3}[H] + k_{f4}[C_2H_2] + k_{f5}[O_2] + k_{f1}[H] + k_{f2}[OH]} \chi_{sootCH}, \quad (81)$$

where χ_{sootCH} is the surface density of hydrogenated sites estimated based on the assumption that soot “surface is assumed to be composed of outwardlooking PAH edges with PAH molecular moieties assembled into turbostratic structures” [98]. Considering the layer spacing of 3.15\AA and 2 C–H bonds per benzene ring length, the surface density of hydrogenated sites, χ_{soot-H} , is calculated to be $0.23\text{site}/\text{\AA}^2 = 2.3 \times 10^{19}\text{site}/\text{m}^2$, which gives the maximum theoretical limit of the reaction sites.

In Equation (79), α is the surface reactivity factor between 0 and 1 that represents the decline of reaction sites from the theoretical limit due to PAH layer orientation, particle aging, growth and maturity [99, 100], and it has been observed to depend on temperature time history [101, 42]. The value of α has been described using constant target-specific values as well as empirical equations based on particle size and flame temperature. A detailed review of these can be found in the chapter 4 of [102]. Here, the empirical equations proposed by Appel et al. [38] is used to calculate α :

$$\alpha^i = \tanh \left(\frac{12.56 - 0.00563 \cdot T}{\log_{10} \left(\frac{\rho_{soot} \cdot Av}{W_{carbon}} \frac{\pi}{6} d_p^3 \right)} - 1.38 + 0.00068 \cdot T \right). \quad (82)$$

Alternatively, Blanquart and Pitsch [39] related α to the number of surface hydrogen atoms on the soot particles.

$$\alpha^i = \frac{H_{tot}^i}{C_{tot}^i}. \quad (83)$$

Table 2: Arrhenius rate coefficients of the various surface reactions in HACA [38], $k = AT^n \cdot e^{-E/RT}$

No.	Reaction		A $\left[\frac{\text{m}^3}{\text{mol}\cdot\text{s}}\right]$	n	$\frac{E}{R}$ [K]
(R 1)	$\text{C}_{\text{soot-H}} + \text{H} \rightleftharpoons \text{C}_{\text{soot}^\circ} + \text{H}_2$	f	4.17×10^7	0	6542.52
		r	3.9×10^6	0	5535.98
(R 2)	$\text{C}_{\text{soot-H}} + \text{OH} \rightleftharpoons \text{C}_{\text{soot}^\circ} + \text{H}_2\text{O}$	f	10^4	0.734	719.68
		r	3.68×10^2	1.139	8605.94
(R 3)	$\text{C}_{\text{soot}^\circ} + \text{H} \longrightarrow \text{C}_{\text{soot}} + \text{H}_2\text{O}$	f	10^4	0.734	719.68
(R 4)	$\text{C}_{\text{soot}^\circ} + \text{C}_2\text{H}_2 \longrightarrow \text{C}_{\text{soot-H}}$	f	80	1.56	1912.43
(R 5)	$\text{C}_{\text{soot}^\circ} + \text{O}_2 \longrightarrow 2 \text{CO}$	f	2.2×10^6	0	3774.53
(R 6)	$\text{C}_{\text{soot-H}} + \text{OH} \longrightarrow \text{CO} + \frac{1}{2} \text{H}_2$	f	1.3×10^7	0	0

The contribution of HACA to growth source terms can be computed from HACA rates considering the number of carbon atoms in C_2H_2 and number of arm-chair and zig-zag hydrogenated sites on soot particle [60] using

$$I_{C_{tot},gr}^i = 2\omega_{gr}^i/\rho, \quad (84)$$

$$I_{H_{tot},gr}^i = 0.25\omega_{gr}^i/\rho. \quad (85)$$

The rate of change of C_2H_2 concentration due to mass growth is written as:

$$\left(\frac{d[\text{C}_2\text{H}_2]}{dt}\right)_{gr} = -\sum_{i=1}^{n_{sec}} \omega_{gr}^i. \quad (86)$$

The rate of release of H radicals into the gas mixture due to surface growth is:

$$\left(\frac{d[\text{H}]}{dt}\right)_{gr} = 1.75 \sum_{i=1}^{n_{sec}} \omega_{gr}^i. \quad (87)$$

The carbons on the surface of soot are oxidized via reaction with O_2 (Reaction 2) and OH (Reaction 2) which decreases total carbon of soot and releases CO and H_2 to gas mixture. The oxidation process is described by HACA mechanism. O_2 and OH oxidation rates are calculated as

$$\omega_{ox,O_2}^i = \alpha^i k_{f5} [\text{O}_2] [\text{C}_{soot^\circ}^i], \quad (88)$$

$$\omega_{ox,OH}^i = \alpha^i k_{f6} [\text{OH}] [\text{soot}^i]. \quad (89)$$

The oxidation source term is calculated considering the number of carbon atoms removed from soot through each oxidation pathway as

$$I_{C_{tot},ox}^i = -(2\omega_{ox,O_2}^i + \omega_{ox,OH}^i)/\rho. \quad (90)$$

We assume that oxidation does not change the number of surface hydrogen atoms. The rate of change of concentration of CO, H and OH by oxidation is calculates as:

$$\left(\frac{d[\text{CO}]}{dt}\right)_{ox} = \sum_{i=1}^{n_{sec}} \omega_{ox,O_2}^i. \quad (91)$$

$$\left(\frac{d[\text{O}_2]}{dt}\right)_{ox} = - \sum_{i=1}^{n_{sec}} \omega_{ox,O_2}^i. \quad (92)$$

$$\left(\frac{d[\text{OH}]}{dt}\right)_{ox} = - \sum_{i=1}^{n_{sec}} \omega_{ox,OH}^i. \quad (93)$$

$$\left(\frac{d[\text{H}_2]}{dt}\right)_{ox} = \frac{1}{2} \sum_{i=1}^{n_{sec}} \omega_{ox,OH}^i. \quad (94)$$

2.5 PAH growth models

Here, four different PAH growth models are implemented to describe the conversion of PAHs to incipient particles and their adsorption on existing agglomerates. As mentioned before, the soot inception and surface growth are not fully understood yet, but there is substantial evidence to support the collision of PAHs as a key step in inception and surface growth [103, 37, 104]. So, global inception models have been developed based PAH collision consisting of different pathways with single or multiple steps. The collision frequency of gaseous species including PAH molecules and polymers depend on their mass and diameter, and it is obtained as:

$$\beta_{dim_{jk}} = 2.2 \cdot d_r^2 \sqrt{\frac{8\pi k_B T}{m_r}}, \quad (95)$$

where $d_{r,PAH}$ and $m_{r,PAH}$ are reduced diameter and mass for two PAH molecules, respectively.

$$d_{r,PAH} = 2 \frac{d_{PAH_k} \cdot d_{PAH_j}}{d_{PAH_k} + d_{PAH_j}}. \quad (96)$$

$$m_{r,PAH} = \frac{m_{PAH_k} \cdot m_{PAH_j}}{m_{PAH_k} + m_{PAH_j}}. \quad (97)$$

The mass of each PAH molecule is obtained from its molecular weight as:

$$m_{PAH_j} = \frac{W_{PAH_j}}{Av}. \quad (98)$$

The diameter of PAH is calculated from its mass and density.

$$d_{PAH_j} = \left(\frac{6 \cdot m_{PAH_j}}{\pi \cdot \rho_{PAH_j}} \right)^{1/3}. \quad (99)$$

The density of a PAH molecule is estimated using the relation proposed by Johansson et al. [105].

$$\rho_{PAH_j} = 171943.5197 \frac{W_{carbon} \cdot n_{C,PAH_j} + W_{hydrogen} \cdot n_{H,PAH_j}}{n_{C,PAH_j} + n_{H,PAH_j}}, \quad (100)$$

where n_{C,PAH_j} and n_{H,PAH_j} denote the number of carbon and hydrogen atoms in j_{th} PAH, respectively. The collision frequency of PAH_j and soot agglomerates in each section can be determined for the entire regime by harmonic mean of the collision frequency in the free molecular and continuum regimes as:

$$\beta_{ads_j}^i = \frac{\beta_{fm,ads}^i \cdot \beta_{cont,ads}^i}{\beta_{fm,ads}^i + \beta_{cont,ads}^i}. \quad (101)$$

$$\beta_{fm,ads_j}^i = 2.2 \sqrt{\frac{\pi k_B T}{2} \left(\frac{1}{m_{agg}^i} + \frac{1}{m_{PAH_j}} \right)} (d_g^i + d_{PAH_j})^2. \quad (102)$$

$$\beta_{cont,ads_j}^i = \frac{2k_B T}{3\mu} \left[\frac{C^i(d_m)}{d_g^i} + \frac{C^i(d_{PAH_j})}{d_{PAH_j}} \right] (d_g + d_{PAH_j}). \quad (103)$$

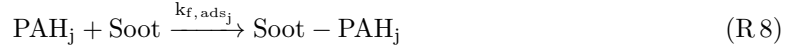
where C^i is the Cunningham function calculated as Equation (34).

2.5.1 Irreversible Dimerization

The irreversible dimerization is based on the irreversible collision of PAHs [38] leading to their clustering/polymerization that forms dimers, trimers, and tetramers until the polymer mass reaches a threshold that can be considered a solid particle. For practical purposes, dimer is usually considered as a incipient particle that grows by surface growth and coagulation. A single-step irreversible collision of two similar PAHs forms a new dimer as:



Similarly, the adsorption of each PAH molecule on soot particles is described by the irreversible collision of soot and PAH_j as:



The forward rate of dimerization, k_{f, dim_j} and adsorption, k_{f, ads_j} in Reactions (R 7) and (R 8) can be calculated as.

$$k_{f, \text{dim}_j} = \gamma_{inc} \cdot \beta_{jk, PAH} \cdot Av, \quad (104)$$

$$k_{f, \text{ads}_j}^i = \gamma_{ads_j} \cdot \beta_{j, ads}^i \cdot Av, \quad (105)$$

$\beta_{jk, PAH}$ and $\beta_{j, ads}^i$ are computed using Equations (95) and (101), respectively, and γ_{inc} and γ_{ads} are the collision efficiencies for dimerization and adsorption, respectively. Their value vary in the range of 10^{-7} to 1, and usually chosen to match the predicted soot mass, volume fraction or size distribution with the experimental data. The default values for γ_{inc} and γ_{ads} are 10^{-4} , and 10^{-3} , respectively. The rate of dimerization and adsorption from PAH_j are calculated accordingly as:

$$w_{\text{dim}_j} = \eta_{inc} k_{f, \text{dim}_j} [\text{PAH}_j] [\text{PAH}_j], \quad (106)$$

where η_{inc} is the inception adjustment factor to globally modify the inception flux without changing the internal rate constants of the inception model. The partial source terms for inception are calculated as:

$$I_{N, inc} = \frac{1}{\rho} \sum_{j=1}^{n_{PAH}} w_{\text{dim}_j} 2n_{PAH_j, C}. \quad (107)$$

$$I_{C_{tot}, inc} = \frac{1}{\rho} \sum_{j=1}^{n_{PAH}} w_{\text{dim}_j} 2n_{PAH_j, C}. \quad (108)$$

$$I_{H_{tot}, inc} = \frac{1}{\rho} \sum_{j=1}^{n_{PAH}} w_{\text{dim}_j} 2n_{PAH_j, H} \quad (109)$$

The rate of PAH adsorption for each section is obtained as:

$$w_{ads_j}^i = \eta_{ads} k_{f, ads_j}^i [\text{soot}] [\text{PAH}_j], \quad (110)$$

where η_{ads} similar to Equation (106) is the adsorption adjustment factor to globally modify the PAH adsorption rate. The contribution of PAH adsorption to the source terms are expressed as:

$$I_{C_{tot},ads}^i = \frac{1}{\rho} \sum_{j=1}^{n_{PAH}} w_{ads_j}^i n_{PAH,C} \quad (111)$$

$$I_{H_{tot},ads}^i = \frac{1}{\rho} \sum_{j=1}^{n_{PAH}} w_{dim_j}^i (n_{PAH,H} - 2) \quad (112)$$

Each PAH molecule loses one H atom becoming a radical that forms bonds with a dehydrogenated site on soot surface, so two H atoms are released during inception that is taken into account in Equation (112).

The formation of a dimer consumes two PAH molecules, and during adsorption one PAH molecule is removed from the gas mixture, so the total rate of PAH_i removal by the irreversible dimerization is obtained as:

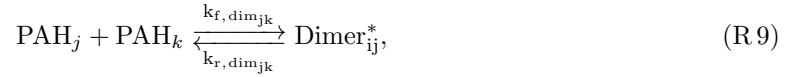
$$\left(\frac{d[\text{PAH}_j]}{dt} \right)_{inc} = -2w_{dim_j} - \sum_{i=1}^{n_{sec}} w_{ads_j}^i. \quad (113)$$

During the adsorption process one H₂ is released to the gas mixture.

$$\left(\frac{d[\text{H}_2]}{dt} \right)_{inc} = \sum_{i=1}^{n_{sec}} w_{ads_j}^i. \quad (114)$$

2.5.2 Reactive Dimerization

This model is built on Irreversible Dimerization, but the first step of dimerization and adsorption is reversible forming physically bonded dimers followed by a irreversible carbonization step that leads to chemical bond formation in dimers [35]. The dimerization of PAH_j and PAH_k is described as:



where Dimer_{ij}^* and Dimer_{jk} are physically and chemically bonded dimers, respectively, from PAH_j and PAH_k. The forward rate of physical dimerization, $k_{f,dim_{jk}}$ is calculated from Equation (95) as:

$$k_{f,dim_{jk}} = p'' \cdot \beta_{jk,PAH} \cdot Av, \quad (115)$$

where $p'' = 0.1$ accounts for the probability of PAH-PAH collisions in “FACE” configuration that results in successful vdW bond formation [106]. The reverse rate of physical dimerization, $k_{r,dim_{jk}}$ is obtained from the dimerization equilibrium constant [107] as:

$$\log_{10} K_{eq} = a \frac{\epsilon_{jk}}{RT} + b, \quad (116)$$

$$k_{r,dim_{jk}} = k_{f,dim_{jk}} 10^{-b} e^{-a\epsilon_{jk} \ln(10)/(RT)}, \quad (117)$$

$$\epsilon_{jk} = cW_{jk} - d, \quad (118)$$

$$W_{jk} = \frac{W_j \cdot W_k}{W_j + W_k}, \quad (119)$$

where $a = 0.115$ (obtained from pyrere dimerization data [30]) and $b = 1.8$ [35], $c = 933420$ j/kg, and $d = 34053$ j/mol [35].

The rate of chemical bond formation, k_{reac} is defined in the Arrhenius form [31] as:

$$k_{reac} = 5 \times 10^6 \cdot e^{(-96232/RT)}. \quad (120)$$

Assuming a steady state condition for the physical dimers, $\partial[\text{Dimer}_{jk}^*]/\partial t = 0$, the rate of formation of chemically-bonded dimers can be obtained as:

$$\omega_{dim_{jk}} = \eta_{inc} k_{reac} \frac{k_{f,dim_{jk}} [\text{PAH}_j] [\text{PAH}_k]}{k_{r,dim_{jk}} + k_{c,dim}}. \quad (121)$$

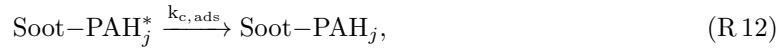
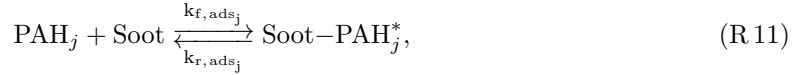
The contribution of dimer formation to partial source terms is expressed by looping over all combinations of PAHs as:

$$I_{N,inc} = \frac{1}{\rho} \sum_{j=1}^{n_{PAH}} \sum_{k=j}^{n_{PAH}} \omega_{dim_{kj}} (n_{PAH_j,C} + n_{PAH_k,C}), \quad (122)$$

$$I_{C_{tot},inc} = \frac{1}{\rho} \sum_{j=1}^{n_{PAH}} \sum_{k=j}^{n_{PAH}} \omega_{dim_{kj}} (n_{PAH_j,C} + n_{PAH_k,C}), \quad (123)$$

$$I_{H_{tot},inc} = \frac{1}{\rho} \sum_{j=1}^{n_{PAH}} \sum_{k=j}^{n_{PAH}} \omega_{dim_{kj}} (n_{PAH_j,H} + n_{PAH_k,H}), \quad (124)$$

Similarly, PAH adsorption is described by a two-step process where the collision of PAH_j with soot agglomerates leads to physically bonded Soot – PAH^* that is carbonized and forms chemically-bonded Soot – PAH added to soot surface.



The forward rate of PAH-soot collision is calculated from Equation (101), and the reverse rate is determined same as inception (Equation (117)).

$$k_{f,ads}^i = \beta_{jk,ads}^i \cdot Av, \quad (125)$$

$$k_{r,ads}^i = k_{f,ads}^i \cdot 10^{-b} e^{-a\epsilon_{soot,j} \ln(10)/(RT)}, \quad (126)$$

$$\epsilon_{soot,j} = cMW_{soot,j} - d, \quad (127)$$

The values of a, b, c, d are the same as those used in inception. Computing $\epsilon_{soot,j}$ also requires “equivalent soot molecular weight”, W_{soot} for section i , which is estimated from carbon mass of each agglomerate as:

$$W_{soot}^i = \frac{C_{tot}^i W_{carbon}}{N_{agg}^i} \quad (128)$$

The rate constant of carbonization of Soot – PAH_j^* is defined as in the Arrhenius form similar to inception (Equation (120)). The prefactor is adjusted based on matching the numerical PSD [31] with measurements in the ethylene pyrolysis in a flow reactor [108].

$$k_{c,dim} = 2 \times 10^{10} \cdot e^{(-96232/RT)}. \quad (129)$$

The total adsorption rate can be calculated assuming a steady-state concentration for physically adsorbed PAH on soot, $\partial[\text{Soot} - \text{PAH}^*]/\partial t = 0$ calculated in a similar way to inception flux (Equation (121)) as

$$\omega_{ads_j}^i = \eta_{ads} k_{c,ads} \frac{k_{f,ads_j} [\text{Soot}] [\text{PAH}_j]}{k_{r,ads_j} + k_{c,ads_j}}, \quad (130)$$

The contribution of PAH adsorption rate to partial source terms can be expressed as:

$$I_{C_{tot},ads}^i = \frac{1}{\rho} \sum_{i=1}^{n_{PAH}} \omega_{ads_j}^i n_{C,PAH_j}, \quad (131)$$

$$I_{C_{tot},ads}^i = \frac{1}{\rho} \sum_{i=1}^{n_{PAH}} \omega_{ads_j}^i (n_{H,PAH_j} - 2). \quad (132)$$

The rate of removal of PAH from gas mixture due to adsorption is given as

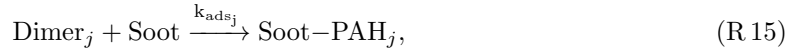
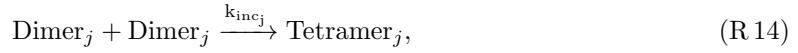
$$\left(\frac{d[\text{PAH}_j]}{dt} \right)_{inc} = - \sum_{k=1}^{n_{PAH}} w_{dim_{jk}} - \sum_{i=1}^{n_{sec}} w_{ads_j}^i. \quad (133)$$

During the adsorption process one H_2 molecule is released to the gas mixture.

$$\left(\frac{d[\text{H}_2]}{dt} \right)_{inc} = \sum_{i=1}^{n_{sec}} w_{ads_j}^i. \quad (134)$$

2.5.3 Dimer Coalescence

Dimer coalescence model is a multi-step irreversible model proposed by Blanquart and Pitsch [39] where self-collision of PAH molecules form dimers that are intermediate state between gaseous PAH molecules and solid soot particles. The dimers can either form incipient soot particles through self-coalescence or adsorb on the surface of existing soot particles and contribute to their surface growth. The following equations describing the inception and surface growth in Dimer Coalescence adopted from the work of Sun et al. [109].



where the rate constant of dimerization, k_{dim_j} , and inception, k_{inc_j} , are calculated from the collision rate of PAHs in Equation (101) as:

$$k_{dim_j} = \gamma_{dim_j} \cdot \beta_{jj,PAH} \cdot Av, \quad (135)$$

$$k_{inc_j} = \beta_{jj,dimer} \cdot Av, \quad (136)$$

where γ_{dim_j} is the dimerization efficiency that is assumed to scale with fourth power of PAH molecular weight [60] as:

$$\gamma_{dim_j} = C_{N,j} \cdot W_{PAH_j}^4, \quad (137)$$

Blanquart and Pitsch [39] estimated the constant $C_{N,j}$ by comparing the profiles of several PAH species with experimental measurements in a single premixed benzene flame [110], and provided a efficiency values for various PAHs that are listed in Table 1 in [60]. The rate of dimer collision is expressed as:

$$w_{dim_j} = \eta_{inc} k_{inc_j} [\text{Dimer}_j] [\text{Dimer}_j] \quad (138)$$

Similarly, the rate of adsorption of dimers on soot particles is obtained as:

$$w_{ads_j}^i = \eta_{ads} k_{ads_j}^i [\text{soot}]^i [\text{Dimer}_j] \quad (139)$$

Assuming fast dimer consumption leads to the steady-state concentration of dimers that can be determined by solving a quadratic equation as:

$$a_{inc_j} [\text{dimer}]^2 + b_{ads_j} [\text{dimer}] = \omega_{dim,j} \quad (140)$$

$$[\text{Dimer}_j] = \begin{cases} \frac{-b_{ads_j} + \sqrt{\Delta_j}}{2a_{inc_j}}, & \text{if } \Delta_j \geq 0 \\ 0 & \text{if } \Delta_j < 0 \end{cases} \quad (141)$$

$$\Delta_j = b_{ads_j}^2 - 4a_{inc_j} \omega_{dim,j} \quad (142)$$

where $a_{inc_j} = k_{inc_j}$ and b_{ads_j} is calculated by summing the adsorption rate of dimer for all sections and dividing it by the dimer concentration.

$$b_{ads_j} = \sum_{i=1}^{n_{sec}} k_{ads_j}^i [\text{soot}]^i \quad (143)$$

After determining the concentration of each dimer, the contribution of inception and PAH adsorption to source terms of tracked soot variables can be calculated similar to previous inception models considering the number of carbon and hydrogen atoms involved in the process.

$$I_{N,inc} = \frac{1}{\rho} \sum_{j=1}^{n_{PAH}} 4\omega_{inc_j} n_{PAH_j,C}, \quad (144)$$

$$I_{C_{tot},inc} = \frac{1}{\rho} \sum_{j=1}^{n_{PAH}} 4\omega_{inc_j} n_{PAH_j,C}, \quad (145)$$

$$I_{H_{tot},inc} = \frac{1}{\rho} \sum_{j=1}^{n_{PAH}} 4\omega_{inc_j} (n_{PAH_j,H} - 2), \quad (146)$$

$$I_{C_{tot},ads}^i = \frac{1}{\rho} \sum_{i=1}^{n_{PAH}} 2\omega_{ads_j}^i n_{C,PAH_j}, \quad (147)$$

$$I_{H_{tot},ads}^i = \frac{1}{\rho} \sum_{i=1}^{n_{PAH}} 2\omega_{ads_j}^i (n_{H,PAH_j} - 2). \quad (148)$$

The rate of removal of PAHs and release of H_2 molecule due to inception and PAH adsorption is calculated as:

$$\left(\frac{d[\text{PAH}_j]}{dt} \right)_{inc} = -4 \sum_{k=1}^{n_{PAH}} w_{inc_j} - 2 \sum_{i=1}^{n_{sec}} w_{ads_j}^i. \quad (149)$$

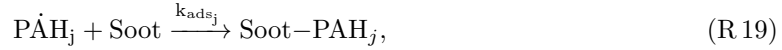
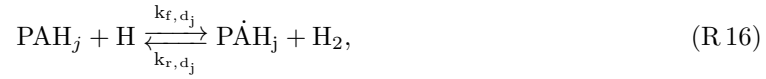
$$\left(\frac{d[H_2]}{dt} \right)_{inc} = 2 \sum_{i=1}^{n_{sec}} w_{ads_j}^i. \quad (150)$$

Table 3: Rate coefficients for the monomer de-/hydrogenation reaction of E-Bridge Modified in Arrhenius form $k = AT^n \cdot e^{-E/RT}$ [36]

Reaction		A $\left[\frac{\text{m}^3}{\text{mol}\cdot\text{s}}\right]$	n	$\frac{E}{R}$ [K]
(R 16)	f	$98 \times n_{C,PAH_j}$	1.8	7,563.519
	r	1.6×10^{-2}	2.63	2145.346
(R 17)	f	4.8658×10^7	0.13	0.0

2.5.4 E-Bridge Modified

The E-Bridge Formation was originally proposed by Frenklach and Mebel [36] to describe soot inception using a HACA-like scheme that starts with dehydrogenation of PAH monomers, often pyrene, which forms the monomer radicals and continues with of sequential addition of the radicals to PAHs that form dimers, trimers and larger polymers until the PAH structure reaches the mass threshold and the clustering process becomes irreversible. Here, a modified version of E-Bridge Formation model is used where dimers are considered as incipient soot, and monomer radical are adsorbed on soot agglomerates. This PAH growth model is described using the following set of pathways:



The rate constants of Reactions (R 16) and (R 17) are listed in Table 3 while those of dimer production and adsorption are calculated based on Equations (95) and (101), respectively. For both steps, it is assumed the all collisions are successful i.e. 100% collision efficiency for radical-monomer and radical-soot.

$$k_{inc_j} = \beta_{jj,PAH} \cdot Av, \quad (151)$$

$$k_{ads_j}^i = \beta_{ads_j}^i \cdot Av, \quad (152)$$

The rate of dimer formation and adsorption is calculated as:

$$w_{dim_j} = \eta_{inc} k_{inc_j} [PAH_j] [\dot{P}AH_j] \quad (153)$$

$$w_{ads_j}^i = \eta_{ads} k_{ads_j}^i [\text{Soot}]^i [\dot{P}AH_j] \quad (154)$$

The calculations of rate of inception and PAH adsorption from PAH_j requires the concentration of corresponding monomer radical that can be determined by applying the steady-state assumption for $\dot{P}AH_j$.

$$\frac{d[\dot{P}AH_j]}{dt} = 0 \quad (155)$$

$$k_{f,d_j}[\text{PAH}_j][\text{H}] - k_{r,d_j}[\dot{\text{PAH}}_j][\text{H}_2] - k_{f,h_j}[\dot{\text{PAH}}_j][\text{H}] - k_{inc_j}[\dot{\text{PAH}}_j]^2 - \sum_{i=1}^{n_{sec}} k_{ads_j}^i[\dot{\text{PAH}}_j][\text{Soot}]^i = 0 \quad (156)$$

The above equations can be rearranged as a quadratic equation similar to the dimer coalescence.

$$a_{inc_j}[\dot{\text{PAH}}_j]^2 + b_{ads_j}[\dot{\text{PAH}}_j] + c_j = 0, \quad (157)$$

$$a_{inc_j} = k_{f,d_j} \quad (158)$$

$$b_{ads_j} = k_{r,d_j}[\text{H}_2] + k_{f,h_j}[\text{H}] + \sum_{i=1}^{n_{sec}} k_{ads_j}^i[\text{Soot}]^i \quad (159)$$

$$c_{inc_j} = k_{f,d_j}[\text{PAH}_j][\text{H}] \quad (160)$$

Finally, solving the quadratic equation for each PAH results in concentration of the radical using the following equation as:

$$[\dot{\text{PAH}}_j] = \begin{cases} \frac{-b_{ads_j} + \sqrt{\Delta_j}}{2a_{inc_j}}, & \text{if } \Delta_j \geq 0 \\ 0 & \text{if } \Delta_j < 0 \end{cases} \quad (161)$$

$$\Delta_j = b_{ads_j}^2 - 4a_{inc_j}c_j \quad (162)$$

The contribution of inception and adsorption to the partial source terms for E-Bridge Modified can be written as:

$$I_{N,inc} = \frac{1}{\rho} \sum_{j=1}^{n_{PAH}} 2\omega_{inc_j} n_{PAH_j,C}, \quad (163)$$

$$I_{C_{tot},inc} = \frac{1}{\rho} \sum_{j=1}^{n_{PAH}} 2\omega_{inc_j} n_{PAH_j,C}, \quad (164)$$

$$I_{H_{tot},inc} = \frac{1}{\rho} \sum_{j=1}^{n_{PAH}} 2\omega_{inc_j} (n_{PAH_j,H} - 2), \quad (165)$$

$$I_{C_{tot},ads}^i = \frac{1}{\rho} \sum_{i=1}^{n_{PAH}} \omega_{ads_j}^i n_{C,PAH_j}, \quad (166)$$

$$I_{H_{tot},ads}^i = \frac{1}{\rho} \sum_{i=1}^{n_{PAH}} \omega_{ads_j}^i (n_{H,PAH_j} - 2). \quad (167)$$

The rate of removal of each PAH involved in soot inception and PAH adsorption and release of H_2 to the gas mixture can be expressed as:

$$\left(\frac{d[\text{PAH}_j]}{dt} \right)_{inc} = -2 \sum_{k=1}^{n_{PAH}} w_{inc_j} - \sum_{i=1}^{n_{sec}} w_{ads_j}^i. \quad (168)$$

$$\left(\frac{d[\text{H}_2]}{dt} \right)_{inc} = \sum_{i=1}^{n_{sec}} w_{ads_j}^i. \quad (169)$$

3 Code Validation

A set of simulations was performed to ensure the accuracy and reliability of omnisooot for prediction of soot formation. Aerosol dynamics is validated by comparing the results of population balance models implemented in omnisooot with those of DEM simulations from literature. Carbon and hydrogen mass and energy balance is also rigorously evaluated to ensure that residuals fall within the bounds of acceptable numerical error.

3.1 Coagulation

A test case¹ was designed and conducted to validate the coagulation sub-model of both particle dynamics models, MPBM and SPBM, in the free molecular regime by comparing the results of omnisooot with those of DEM [111]. The constant volume reactor was used for this test case, but it will be applicable to other reactors and flame models as long as the particle residence time matches with the values obtained by DEM. An adiabatic reactor with the volume of 1 m³ is initialized with 2.6261×10^{18} spherical particles 2 nm in diameter. The initial conditions are indicated in Table 4. The particles coagulate in the free molecular regime and grow in size without inception and surface growth. Figure 7 demonstrates N_{agg} , N_{pri} , d_m , d_g of particles obtained by omnisooot that are in good agreement with DEM results [111]. N_{pri} is conserved during coagulation resulting in identical flat lines for both particle dynamics models, but N_{agg} declines over time with the higher decay rate for SPBM because it accounts for the polydispersity of agglomerates that results in larger collision frequency compared to MPBM. Therefore, mean mobility and gyration diameter of SPBM (red lines in Figure 7b) are slightly larger than those of MPBM (blue line of the same figure).

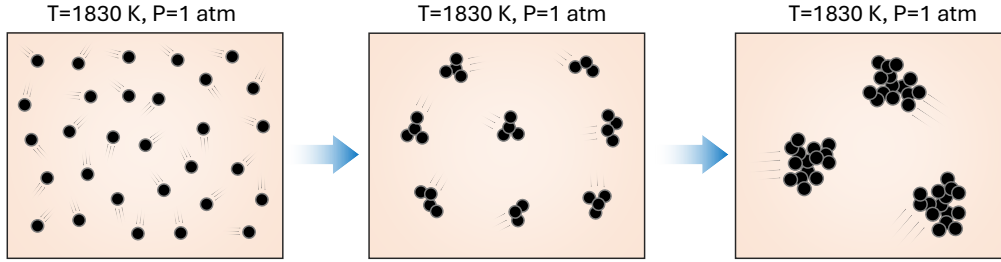


Figure 6: The schematic of agglomeration process in the coagulation test cases where initially spherical particle collide and form agglomerate

MPBM model cannot resolve PSD because of the monodispersity assumption. In contrast, SPBM tracks the number concentration of particles in separate sections that can be used to construct evolving PSD and calculate mean properties and determine the spread of size distribution of particles during coagulation. Figure 8a shows the standard deviation of mobility diameter, σ_g , predicted by SPBM in close agreement with DEM results. σ_g starts from unity indicating a monodisperse population at the beginning of simulation, and it finally reaches 2.03 that is the signature standard deviation of the free molecular regime [112]. Figure 8 demonstrates the evolution of non-dimensional PSD from $t = 1$ ms to 677 ms. The PSD is plotted for the normalized concentration, $\Psi = \bar{v} n_{agg}(v, t) / N_{agg, \infty}$ and dimensionless volume, $\eta = v / \bar{v}$, where $n_{agg}(v, t)$ is the size distribution function of agglomerate, v particle volume, \bar{v} mean particle volume, $N_{agg, \infty}$ total number concentration of agglomerates. For short residence times, $t \approx 4$ ms, the PSD resembles a half bell curve because the majority of particles has sizes close to $d_0 = 2$ nm with the average volume close to the minimum volume, so the particles with $\eta \approx 1$ has the largest concentration. As particles grow by coagulation, the PSD rapidly transitions to a full bell-curve ($t \geq 22$ ms) and does not change for longer residence times, $t \geq 447$ ms marking the attainment of SPSPD in a good agreement with DEM results. This confirms the

¹https://github.com/mohammadadib-cu/omnisooot-cv/tree/main/validations/coagulation/free_molecular

Table 4: The simulations conditions of the coagulation test case [111]

Property	Value
Composition	CH ₄ :0.425, O ₂ :0.435, N ₂ :0.14
T	1830 K
P	1 atm
N_{agg}^1	3.514×10^{-5} mol/kg
N_{pri}^1	3.514×10^{-5} mol/kg
d_p^1	2 nm

capability of SPBM implemented in omnisoot to capture SPSP for soot agglomerates as a signature of Brownian-driven particle coagulation.

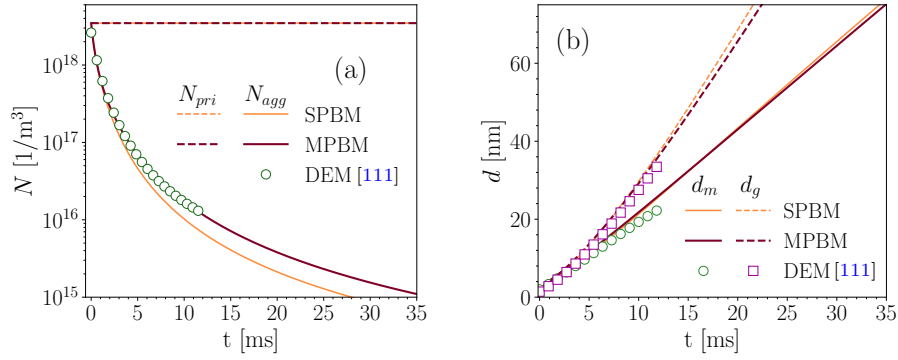


Figure 7: The total number concentration of agglomerates and primary particles (a), and mobility and gyration diameter (b) obtained with omnisoot using MPBM and SPBM that are in close agreement with the DEM results [111] indicating the validation of coagulation sub-model

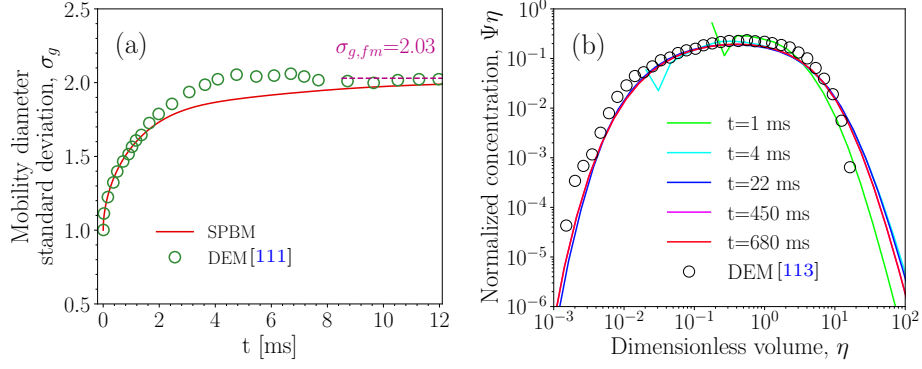


Figure 8: The standard deviation of mobility diameter, σ_g , obtained with SPBM in close agreement with DEM results [111] (shown in the left pane) that reaches $\sigma_{g, fm} = 2.03$ characteristic of the free molecular regime [112]; the particle size distribution normalized number concentration of agglomerates is plotted against non-dimensional volume (shown in the right pane) at different residence times that overlaps after initial transient phase marking the attainment of self-preserving size distribution in good agreement with DEM results [113]

A similar test² was performed in the continuum regime, and the results from the SPBM were compared with those obtained from DEM. The simulation conditions were the same as in the previous case (Table 4), except for the temperature, $T = 600$ K, and the initial particle diameter, $d_p^1 = 259$ nm. Figure 9 shows that the non-dimensional size distribution predicted by SPBM reaches the self-preserving state in good agreement with DEM results [113], which supports the validity of the coagulation sub-model in Omnisoot under continuum conditions.

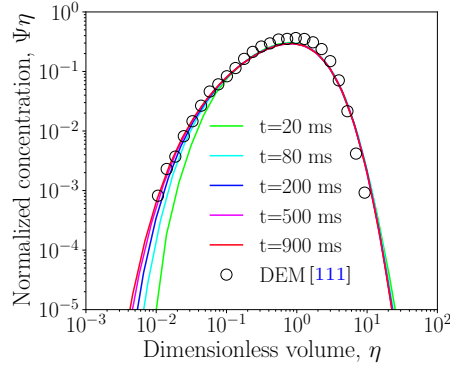


Figure 9: The particle size distribution normalized number concentration of agglomerates plotted against non-dimensional volume reaches self-preserving size distribution in good agreement with DEM results [113]

3.2 Elemental and Energy Balance Assessment

To ensure the accuracy and reliability of the simulations, the conservation of elemental mass and energy was assessed across all reactor models implemented in omnisoot. Elemental balances of carbon and hydrogen, as well as the total energy (internal or enthalpy depending on the reactor type) of the gas-particle system, were evaluated during soot formation processes under various pyrolysis and combustion conditions. Simulations were performed using different combinations of PAH growth and particle dynamics models, and the relative errors in elemental and energy balances

²<https://github.com/mohammadadib-cu/omnisoot-cv/tree/main/validations/coagulation/continuum>

were monitored over time or reactor length. The residuals for all reactor configurations remained within acceptable limits (typically below 10^{-10}), confirming that omnisoot accurately preserves mass and energy during the coupled evolution of gas-phase and particulate species. The relative error of total carbon, hydrogen and energy in CVR, CPR, PSR, and PFR using different combinations of particle dynamics and inception models is shown in Figures S2-S5.

4 Results and Discussion

4.1 Uncertainties in gas chemistry

Accurate simulation of soot and carbon black formation remains a major challenge due to the compounded uncertainties in both gas-phase chemistry and particle dynamics. One of the central difficulties lies in the limited quantitative understanding of soot inception and surface growth mechanisms. The pathways and rate constants for elementary reactions governing PAH dimerization, radical interactions, and surface reactions are not well established. As a result, any sub-model used to describe soot inception and surface growth introduces significant uncertainties when coupling gas-phase chemistry with particle dynamics.

These uncertainties are built upon those already present in detailed chemical kinetic mechanisms, particularly in predicting intermediate species such as acetylene (C_2H_2) and polycyclic aromatic hydrocarbons (PAHs). Prior studies have shown that the predicted concentrations of large PAHs can vary by orders of magnitude depending on the chosen reaction mechanism. Consequently, soot models inherit uncertainty from two sources: (i) the reaction mechanism used to describe fuel pyrolysis and oxidation, and (ii) the choice of inception and surface growth models and parameters. The cumulative effect significantly complicates efforts to produce reliable predictions of soot mass and morphology.

In contrast, particle dynamics models introduce a relatively low uncertainty when provided with accurate estimates of carbon flux from inception and surface growth. These models, particularly when well-validated, are capable of accurately predicting key particle properties such as volume fraction, size distribution, and agglomerate morphology. This highlights the importance of coupling between gas-phase chemistry and soot formation models: the reliability of soot and carbon black simulations hinges less on the particle dynamics approach itself and more on the accuracy of upstream chemical kinetics, inception and surface growth fluxes.

To illustrate the impact of chemical mechanism selection on precursor formation, a series of simulations³ were performed using the CPR model of omnisoot (with soot formation disabled) for the pyrolysis of 5% CH_4 -Ar mixture at $T_5 = 2200$ K. Seven widely used mechanisms were evaluated: ABF [38], Caltech [115], KAUST [116], CRECK [117], ITV [118], NUIG [119], and FFCM2 [120]. These mechanisms have varying degrees of complexity and validation histories, particularly in high-temperature pyrolysis environments.

The comparison focuses on the predicted Carbon Mass Fraction (CMF) of species involved in soot formation. Here, CMF is defined as the mass of carbon in a given species normalized by the total carbon mass in the gas mixture. Initially, the CMF of methane is equal to 1, indicating that all carbon is stored in CH_4 at $t = 0$ in the studied shock tube.

Figure 10 shows the variability in the predicted CMF of CH_4 , C_2H_2 , and A2R5 across different reaction mechanisms. The CMF of CH_4 serves as a useful indicator of carbon flux from the fuel to intermediate species. C_2H_2 is the most abundant hydrocarbon during pyrolysis and plays a key role in the HACA mechanism for PAH growth beyond benzene, as well as in surface growth of soot. A2R5 has been identified as important for soot inception due to its propensity for radical interaction and molecular stacking [121].

As shown in the inset of Figure 10a, the CRECK mechanism predicts the highest CH_4 conversion up to 1 ms, but this trend reverses at longer residence times, where KAUST predicts the lowest CMF. ABF, FFCM2 and NUIG underpredict the methane conversion rate by nearly 10% of the

³https://github.com/mohammadadib-cu/omnisoot-cv/tree/main/examples/pressure/mechanism_comparison

initial carbon compared to the other mechanisms. As expected, the majority (60–80%) of the initial carbon is converted to C_2H_2 by the end of the simulation. In the inset of Figure 10b, all mechanisms direct more carbon toward C_2H_2 by 5 ms. CRECK predicts the highest C_2H_2 CMF up to 3.5 ms, after which NUIG and FFCM2 gives the largest C_2H_2 CMF. This is attributed to FFCM2 and NUIG’s lack of aromatic and large hydrocarbon species, so it does not account for the conversion of C_2H_2 to PAHs.

The relative difference between the mechanisms is most pronounced for A2R5, spanning over an order of magnitude between ABF and KAUST. This aligns with previous findings that the uncertainty in the predicted concentration of gas-phase species increases with molecular size [114]. This highlights the escalating uncertainty with increasing molecular size of PAHs and reinforces that any inception model built on these predictions inherits and amplifies such uncertainties.

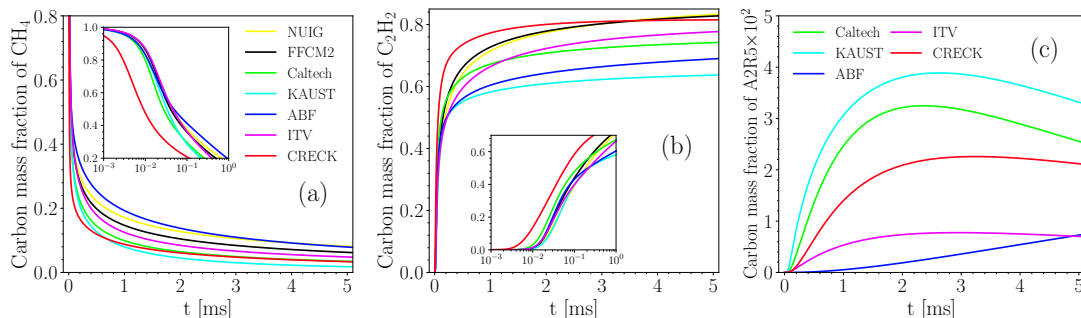


Figure 10: The carbon mass fraction of CH_4 (a), C_2H_2 (b), and A2R5 (c) during pyrolysis of 10% CH_4 -Ar predicted using different reaction mechanisms. The insets provide a zoomed-in view of the early-time behavior

The uncertainties in the precursors chemistry coupled with the poorly constrained pathways for soot inception and surface growth results in the compounded uncertainty that changes soot yield, particle number concentration and characteristic diameters by orders of magnitude depending on the temperature, pressure and fuel composition in studied targets. For these reasons, we avoid evaluating inception models based on their absolute accuracy. Instead, we selected reaction mechanisms that provide enough carbon flux to soot precursors (listed in Table 1) that allows adjusting inception and surface growth flux using the corresponding factors (η_{inc} and η_{ads}) to match simulated soot volume fraction, particle size (e.g., d_p or d_m), or PSD. Among the mechanisms tested, only the Caltech, KAUST, and ITV models met these criteria. The ITV mechanism, however, was not used in this study due to its large size (759 species and 7582 reactions), which makes it too computationally expensive for parametric studies.

It should be noted that the calibration process does not resolve the mechanistic uncertainties of soot formation. It allows the model to back-calculate effective carbon fluxes from the gas phase into the particle phase that are consistent with measured soot characteristics. When combined with a well-validated particle dynamics model, this approach provides a robust means of quantifying the net impact of chemistry and bridging the uncertainty gap between molecular-scale kinetics and macroscale soot morphology.

4.2 Methane pyrolysis in shock-tube

The pyrolysis of a 5% CH_4 -Ar mixture was investigated using the CPR model over a post-shock temperature range $T_5 = 1800$ – 3000 K and a pressure range $P_5 = 4.7$ – 7.1 bar. Since P_5 was not specified for each experiment (characterized by a given T_5), we assumed a linear increase of P_5 with T_5 within the specified range [122]. The Caltech mechanism was used to describe gas-phase chemistry. Inception and PAH adsorption rates were adjusted using η_{inc} and η_{ads} , respectively, to match the predicted Carbon Yield, CY, at $t = 1.5$ ms with light extinction measurements at $\lambda = 632$

nm over the studied T_5 and P_5 ranges [122]. The measured CY was retrieved from the reported product $CY \times E(m)$. There are uncertainties in CY calculated using this technique due to variability in $E(m)$. It is common to use the $E(m)$ of mature soot, which may not be accurate for soot particles formed in a shock tube over short residence times (≈ 2 ms). $E(m)$ increases significantly with particle size, composition, and maturity. For example, $E(m)$ varies from 0.05 to 0.25 as the primary particle diameter grows to 20 nm within 1.6 ms during acetylene pyrolysis. However, there remains a substantial gap in our quantitative understanding of evolving $E(m)$ values for soot. We considered the reported variability of $E(m)$ in the literature, ranging from 0.174 [123] to 0.37 [124].

A parametric study was conducted on η_{inc} and η_{ads} using a grid search approach. Each factor was varied across 11 logarithmically spaced values from 10^{-4} to 1, resulting in 121 simulation cases per data point (847 simulations in total). Combinations of η_{inc} and η_{ads} were ranked by the average relative error across all data points (over the entire studied T_5 range) to identify the set of adjustment factors that minimized the CY prediction error. Figure 11 shows a heat map of the mean relative error, normalized by the maximum value, for all inception models. The largest error occurs for the combination of maximum inception ($\eta_{inc} = 1$ or $\log_{10}(\eta_{inc}) = 0$) and minimum adsorption ($\eta_{ads} = 10^{-4}$ or $\log_{10}(\eta_{ads}) = -4$). The region of lowest normalized error (less than 5%) (outlined in blue in Figure 11) includes a broad set of adjustment factor combinations that enable the model to accurately predict CY. Among those, three types of combinations are of interest: where (i) the minimum inception flux (i.e., $\eta_{inc} = 10^{-4}$), (ii) the minimum PAH adsorption rate (i.e., $\eta_{ads} = 10^{-4}$) (iii) the equally scaled inception flux and the PAH adsorption rate ($\eta_{inc} \approx \eta_{ads}$). All three combinations result in low CY prediction error but may affect predicted soot morphology. To better understand these effects, we adopted a multi-step approach: (i) simulations without soot were performed to isolate gas-phase chemistry and C_2H_2 formation; (ii) inception models were optimized using equal adjustment factors $\eta_{inc} = \eta_{ads}$; and (iii) separate optimizations were performed for minimum adsorption ($\eta_{ads} = 10^{-4}$) and minimum inception ($\eta_{inc} = 10^{-4}$), denoted as *Min Ads* and *Min Inc*, respectively.

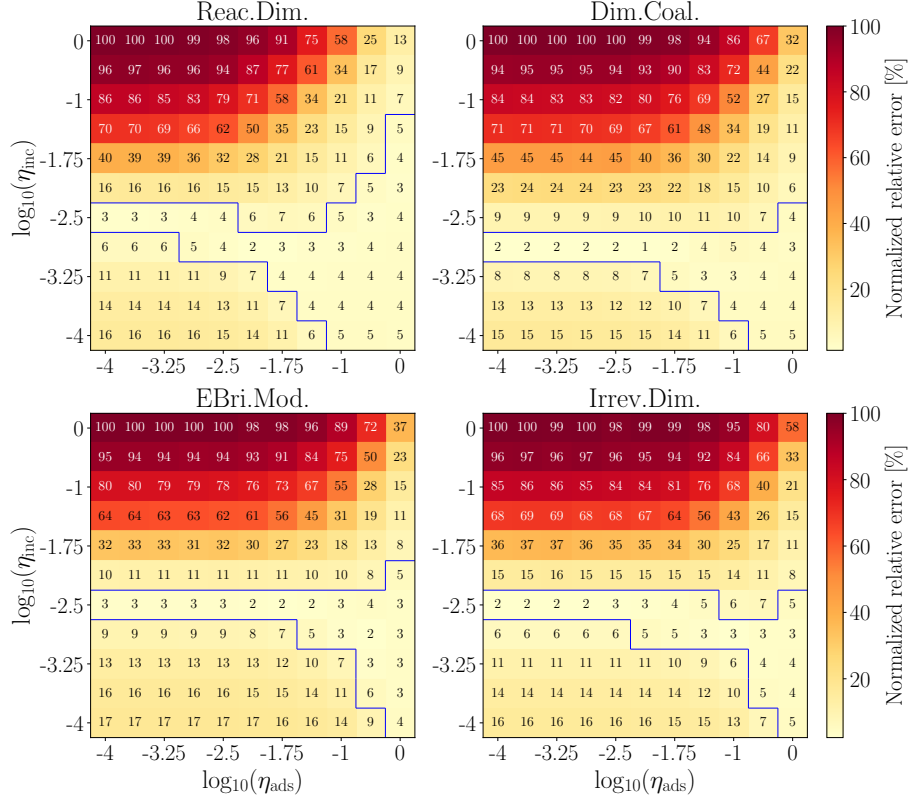


Figure 11: The relative error of CY normalized by the maximum value at $t = 1.5$ ms for 5% CH_4 obtained using Caltech mechanism and different inception models.

Figure 12a shows the CMF of soot precursors (individual PAHs and total) and C_2H_2 at 1.5 ms across the studied temperature range, with the soot model deactivated. While PAH precursors exhibit a bell-shaped profile, the CMF of C_2H_2 increases linearly with temperature and plateaus near 85% at $T_5 \approx 2400$ K. Among the considered PAHs, A2, A2R5, and A4R5 account for most of the carbon and are likely major contributors to soot inception and surface growth. The significant variation in PAH CMF highlights the impact of precursor selection on inception flux, surface growth rates, and their temperature sensitivity. Figure S7 illustrates the effect of excluding five-membered ring PAHs (A2R5, A3R5, and A4R5) from the soot precursors on the CY and d_p . As expected, excluding these species leads to a substantial reduction in CY: a factor of 3 for Reactive Dimerization and a factor of 12 for E-Bridge Modified model. The peak CY temperature remains nearly unchanged for E-Bridge Modified model but shifts to 2100 K for other inception models. The impact on d_p is less pronounced, showing a decrease for Reactive Dimerization and a slight increase for other models in the 2100 – 2500 K range.

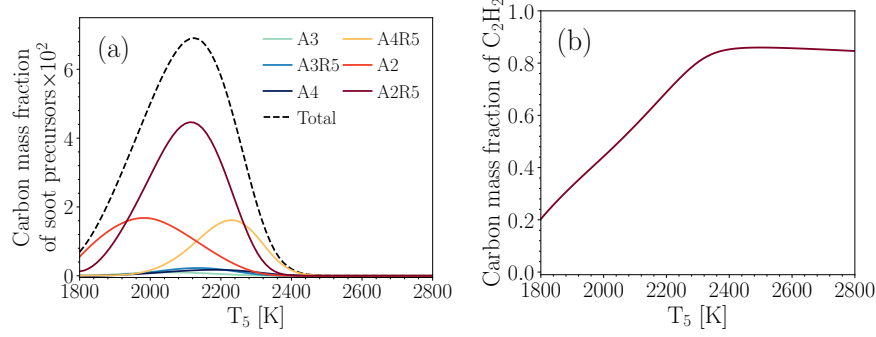


Figure 12: The bell-shape temperature profile of carbon mass fraction of soot precursors (A2 and larger) combined (a) and C_2H_2 (b) at $t = 1.5$ ms during pyrolysis of 5% (red line) and 10% CH_4 -Ar (green line) obtained using CPR model with Caltech mechanism without considering soot.

Next set of simulations were conducted by using equal adjustment factors ($\eta_{inc} = \eta_{ads}$) to minimize the prediction error of CY. Figure 13 compares CY and d_p from various inception models with experimental extinction data [122]. A skew exponential curve (black dotted line) was fitted to highlight the CY trend and its peak near 12%. Soot CY follows a bell-shaped profile similar to that of soot precursors, as inception flux and mass growth directly depend on precursor concentrations. Reactive Dimerization predicts higher CY at lower temperatures, while E-Bridge Modified model shifts the peak to higher temperatures due to a different temperature dependency—primarily governed by PAH dehydrogenation via an Arrhenius rate law, in contrast to physical PAH collisions in other models. The predicted d_p increases with T_5 , reaching a maximum of 12.5 nm at 2700 K, where yield is minimal ($\approx 10^{-7}$), and then drops to the model's minimum allowed value of 2 nm. Figure 14a shows that N_{pri} peaks at ≈ 2200 K, aligning with the peak in CY. This is expected since N_{pri} depends solely on the inception flux, which is highest when PAH concentrations peak. Increased coagulation rates reduce N_{agg} in the 2000 – 2500 K range. Reactive Dimerization model yields the fewest particles (N_{pri} and N_{agg}) because more precursors are directed toward surface growth. Consequently, n_p is lowest for Reactive Dimerization model. Differences between inception models are more evident in n_p than in d_p , influencing predicted particle morphology. These differences become more pronounced at longer residence times. For instance, Dimer Coalescence model predicts a more ramified agglomerate ($n_p = 38$) compared to Reactive Dimerization model ($n_p = 12$). Additional morphological data could help constrain inception and surface growth rates in soot models.

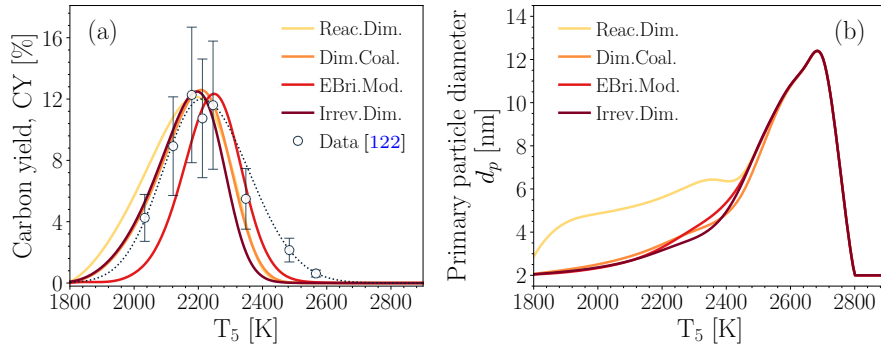


Figure 13: The bell-shape temperature profile of CY at $t = 1.5$ ms (a) and increasing primary particle diameter, d_p , obtained using Caltech mechanism and different inception models optimized using equal adjustment factors to minimize the prediction with extinction measurements [122]. The dashed line was added to show the trend in the measurements.

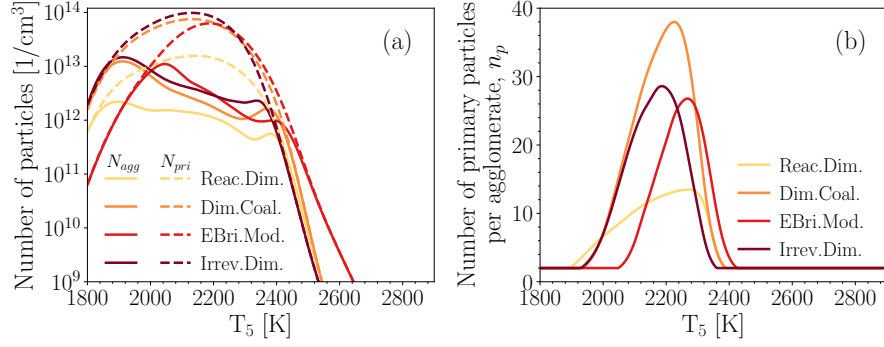


Figure 14: The temperature dependence of total number of agglomerates, N_{agg} (a), number of primary particles per agglomerate, n_p (b) at $t = 1.5$ ms obtained using Caltech mechanism and different inception models optimized using equal adjustment factors to minimize the prediction with extinction measurements [122].

The differences between inception models in prediction of d_p is overall negligible except for Reactive Dimerization model, which predicts a larger d_p in $T_5 < 2500$. The d_p trends can be better understood by examining Equation (25) indicating that d_p is proportional of the third-root of C_{tot}/N_{pri} . C_{tot} describes total carbon mass converted to soot through inception and surface growth while N_{pri} is only determined by inception flux. As a result, d_p is controlled by the ratio of surface growth (HACA and PAH adsorption) rate to inception flux. The ratio of carbon mass gained up to 1.5 ms by each pathway to the total soot carbon mass is calculated and shown in Figure 15. PAH adsorption is the dominant soot mass growth pathway for Reactive Dimerization model in $T_5 < 2000$ K (Figure 15a) that results in larger C_{tot}/N_{pri} and d_p values, but inception is dominant for the other inception models. The CMF of inception decreases with temperature for all inception models leading to higher d_p values up to 2700 K and it increases afterwards that changes d_p trends.

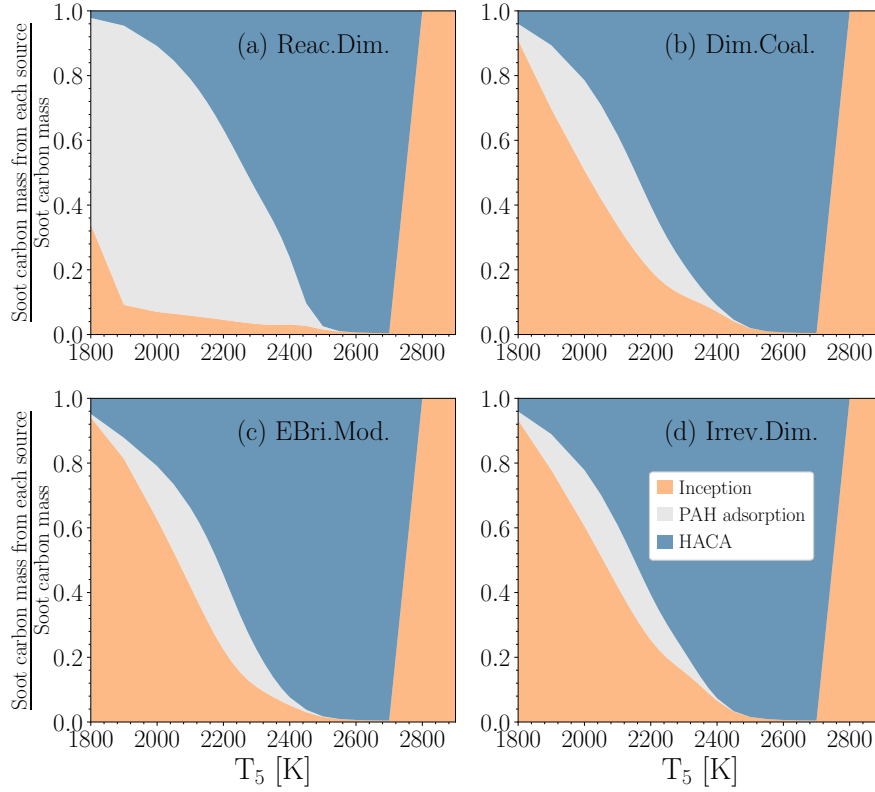


Figure 15: The soot carbon mass from inception, PAH adsorption and HACA normalized by total soot carbon mass at $t = 1.5$ ms for 5% in Ar obtained using Caltech mechanism and different inception models calibrated to minimize the prediction with extinction measurements [122].

Figure 16 shows that optimizing models with minimum η_{inc} and η_{ads} yields similar CY predictions across inception models, except E-Bridge Modified model, which shifts slightly toward higher temperatures. The minimum adsorption case has a higher peak and narrower profile compared to the minimum inception case. Figure 17 demonstrates the variation in d_p among the inception models with the minimum inception (solid line) mode compared to the minimum adsorption (dashed line) that show negligible sensitivity to the inception model. In the minimum inception mode, the majority of soot mass comes from PAHs, so d_p shows a bell-shape profile with a peak close to the temperature of the peak CMF of precursors (dashed line in Figure 12). Reactive Dimerization model has the largest variation at the peak from 2 to 21 nm for the minimum inception and adsorption, respectively. The global adjustment factors were used to alter the contribution of precursors to inception and surface growth without changing the internal rate constants of inception models. A close agreement was achieved between the predicted and measured CY in different modes of inception and PAH adsorption that can result in different soot morphology. Characterizing primary particle size in the experiment can reduce the uncertainty in the model and restrict the range of expected inception and surface growth rate and highlight the need to account for missing pathways and phenomena involved in soot yield and morphology.

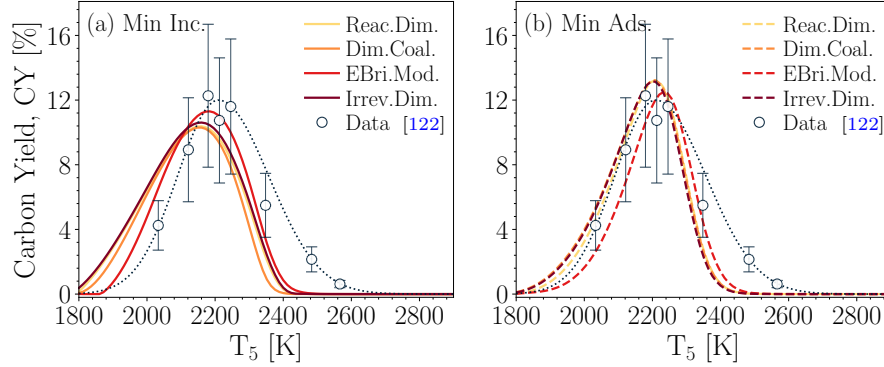


Figure 16: The comparison of CY at $t=1.5$ ms when the minimum inception (a) and the minimum PAH adsorption (b) adjustment factors were applied to minimize the prediction error compared to measurements [122] for 5% CH_4 -Ar obtained using Caltech mechanism and different inception models.

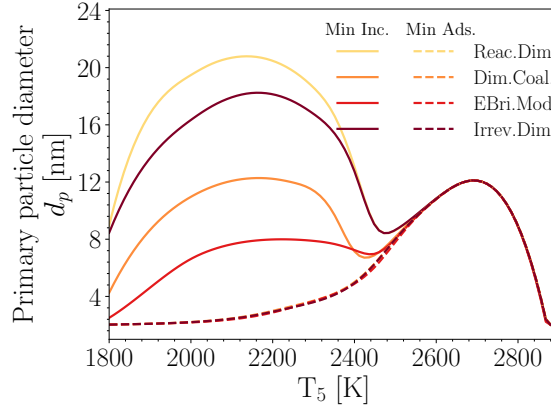


Figure 17: The comparison of mean primary particle, d_p , at $t=1.5$ ms when the minimum inception (solid lines) and adsorption (dashed lines) were applied to minimized the prediction error compared to measurements [122] for 5%-Ar obtained using Caltech mechanism and different inception models.

4.3 Ethylene pyrolysis in a flow reactor

The plug flow reactor (PFR) model was used to simulate the pyrolysis of 0.6% C_2H_4 - N_2 in a 1.4 m-long, 16 mm-diameter flow reactor. Figure 18 shows the axial temperature profile used in the simulations. The maximum temperature, $T_{\text{max}} = 1673$ K, was imposed on the model based on thermocouple measurements reported by Mei et al. [125] for various flow rates along the reactor centerline. The temperature increases from 300 K at the reactor inlet to the hot zone, where it reaches within 10% of T_{max} . The length of the hot zone varies with flow rate due to advection, ranging from 0.71 m at $Q = 8$ L/min to 0.76 m at $Q = 12$ L/min. Near the reactor outlet, the temperature drops to approximately 650 K.

The inception and PAH adsorption adjustment factors were varied to match the predicted PSD with experimental measurements at the reactor exit for flow rates of 8.5, 11, and 12 L/min, as shown in Figure 19. The parametric analysis revealed that each inception model requires a unique set of adjustment factors to minimize the PSD prediction error across different flow rates. The KAUST mechanism [116] was used to describe gas-phase chemistry, as it provided better agreement with the measured PSDs than the Caltech mechanism.

A bimodal size distribution can be observed for $Q=8$ L/min (Figure 19a) that was attributed to the continuous inception [103]. The comparison of simulations with measurements reveals different temperature dependence of inception models. Irreversible Dimerization and Dimer Coalescence models capture the bimodality of PSD in good agreement with the measurements, but the other two models predict a nearly unimodal PSD. The number concentration of the first section is lower by more than three orders of magnitude for Reactive Dimerization and E-Bridge Modified models indicating the lack of active inception at the sampling location due the temperature drops near the end of reactor that suppresses soot inception.

All inception models capture the disappearance of the PSD shoulder at flow rates of 11 and 12 L/min. In these cases, the shorter particle residence time limits coagulation, preventing formation of a second peak. However, Reactive Dimerization and E-Bridge Modified models still underpredict the number concentration of nascent particles by approximately one order of magnitude compared to the irreversible models.

Figure 20 presents the axial evolution of N_{agg} . Predictions from all models agree closely up to $z \approx 1.1$ m, corresponding to the end of the hot zone. Beyond this point, N_{agg} continues to increase for the irreversible models, which allow soot inception to proceed in cooler downstream regions. These models agree well with experimental data at 8 and 11 L/min but tend to overpredict N_{agg} at 12 L/min.

As shown in Figure 21, soot inception flux rises sharply as the gas enters the hot zone. The axial location where the flux exceeds $10^7 \text{ cm}^{-3} \text{ s}^{-1}$ is similar across all inception models, as it is primarily determined by PAH chemistry. However, this location shifts downstream with increasing flow rate due to reduced residence time. Within the hot zone, differences among the inception models are minimal. Outside the hot zone, Irreversible Dimerization and Dimer Coalescence models maintain high inception flux, while Reactive Dimerization and E-Bridge Modified models predict a rapid decrease of more than three orders of magnitude due to cooling. Figure 22 demonstrates the contribution of each pathway to total carbon mass of soot along the reactor that elucidate the link between the balance of inception and surface growth with particle morphology. The relative strength of inception decreases from 100% to less than 5% by $z=1.1$ m for all inception models leading to a gradual increase of d_p and d_m . Irreversible Dimerization and Dimer Coalescence models predict an increase in contribution of inception that resulting in the decline of d_p while Reactive Dimerization and E-Bridge Modified models predict a nearly constant d_p .

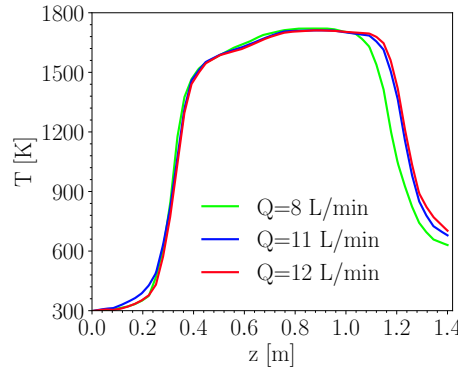


Figure 18: The centerline temperature along the reactor for $Q = 8, 11$, and 12 L/min interpolated from the thermocouple measurements [125].

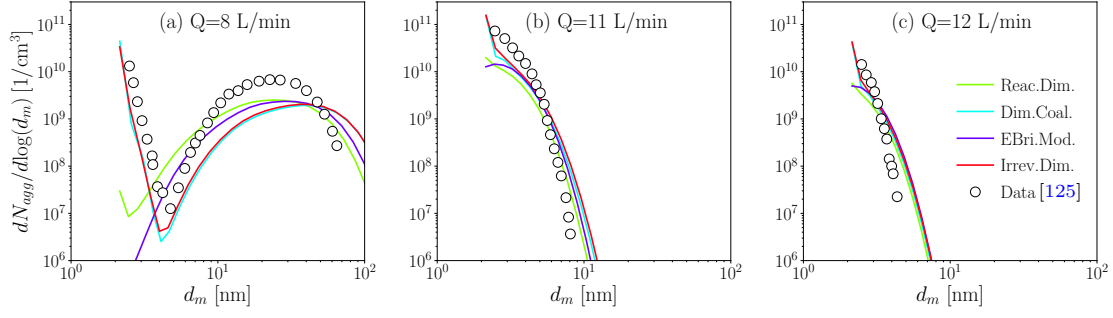


Figure 19: The particle size distribution at the end of PFR for $Q = 8.5$ (a), 11 (b), and 12 L/min (c) obtained using KAUST mechanism and different inception models calibrated to match the predictions with measurement [125].

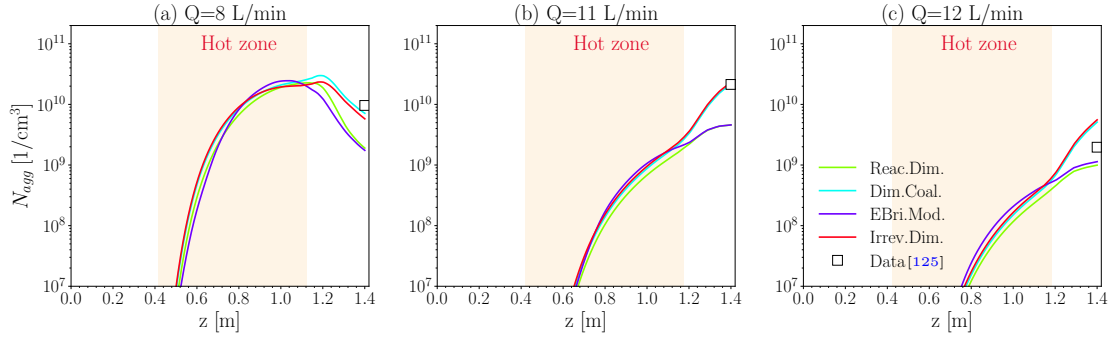


Figure 20: The total number of agglomerates along the PFR for $Q = 8.5$ (a), 11 (b), and 12 L/min (c) obtained using KAUST mechanism and different inception models compared with data [125]. The yellow area represent the region with temperature larger than 1200 K.

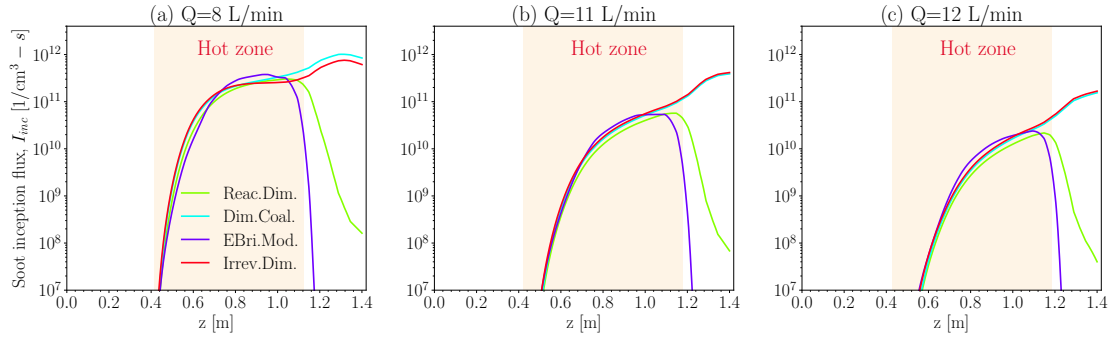


Figure 21: The soot inception flux along the PFR for $Q = 8.5$ (a), 11 (b), and 12 L/min (c) obtained using KAUST mechanism and different inception models. The yellow area represent the region with temperature larger than 1200 K.

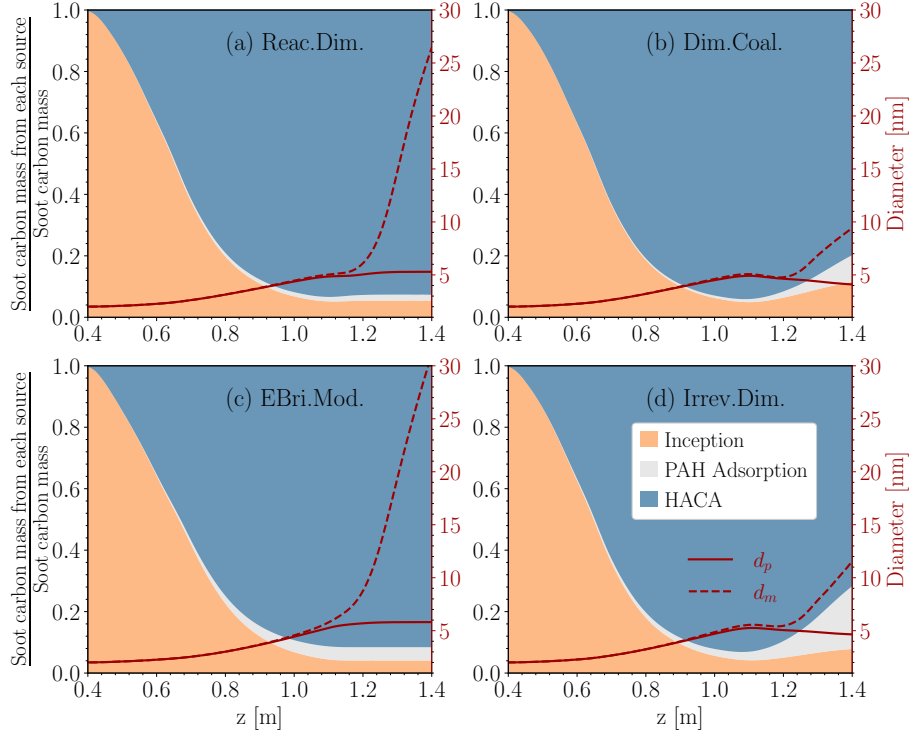


Figure 22: The soot carbon mass from inception, PAH adsorption and HACA normalized by total soot carbon mass for $Q = 8.5$ L/min along with d_p and d_m obtained using KAUST mechanism and different inception models.

4.4 Ethylene oxidation in a perfectly stirred reactor

Manzello et al. [126] utilized a perfectly stirred reactor connected to a flow reactor to study soot formation during ethylene oxidation at different equivalence ratios, $\phi = 1.9, 2.0$, and 2.1 , and provided PSD measurements at the end of flow reactor using Nano-Differential Mobility Analyzer (Nano-DMA). The PSR had the same size of the reactor used by Manzello et al. [126] and explained in Section S3.2. The flow reactor is 70 cm long with an inner diameter of 5.1 cm. A coupled PSR-PFR reactor model of omnisoot was used to simulate soot formation during the combustion and flow evolution in the device. The nominal residence time, τ , of flow in the PSR is 11 ms [126]. The reactants are assumed to enter an adiabatic PSR at 300 K with an inlet mass flow rate of $\dot{m}_{in} = \rho V / \tau$ where ρ was calculated at reactor temperature of 1723 K suggested by Lenhert and Manzello [127]. The calculated average axial velocity in the PFR is 14.5 m/s close to the values suggested by Manzello et al. [126].

KAUST mechanism was used to describe gas chemistry. The inception and PAH adsorption adjustment factors were varied for each PAH growth model to match the predicted PSD with the measurements as closely as possible for all three equivalence ratios. As shown in Figure 23, all inception models capture the peak number concentration and the unimodal shape of the PSD, which indicates that particle inception has ceased, and coagulation is the dominant mechanism for agglomerate size growth. As reported in Table 5, the geometric mean mobility diameter, $d_{m,g}$, and the geometric mobility standard deviation, $\sigma_{m,g}$, obtained using all inception models are in good agreement with the values calculated from the measured PSD [126]. As it can be seen in Figure 23a and b, the spread of predicted PSD is narrower than that of measurements for $\phi = 1.9$ and 2.1 , which corresponds to underprediction of $\sigma_{m,g}$ for these equivalence ratios.

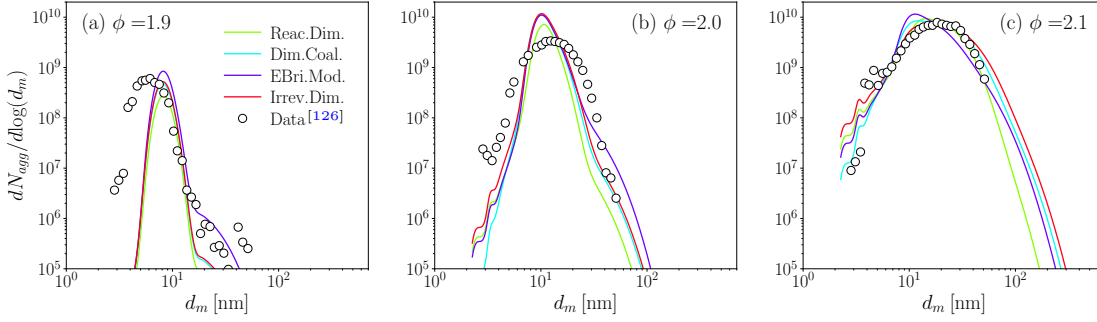


Figure 23: The particle size distribution at the end of PFR for $\phi=1.9$ (a), 2.0 (b), and 2.1 (c) obtained using KAUST mechanism and different inception models calibrated to match the predictions with measurement [126].

Table 5: The geometric mean mobility diameter, $d_{m,g}$, and the geometric mobility standard deviation, $\sigma_{m,g}$, obtained using different inception models compared with the value calculated from the measured PSD [126]

	$\phi=1.9$		$\phi=2.0$		$\phi=2.1$	
	$d_{m,g}$ [nm]	$\sigma_{m,g}$	$d_{m,g}$ [nm]	$\sigma_{m,g}$	$d_{m,g}$ [nm]	$\sigma_{m,g}$
Data [126]	6.04	1.25	12.40	1.49	17.66	1.64
Reactive Dimerization	8.27	1.14	11.10	1.21	16.88	1.58
Dimer Coalescence	8.18	1.14	10.76	1.24	16.99	1.68
E-Bridge Modified	8.27	1.15	11.02	1.27	14.56	1.58
Irreversible Dimerization	8.19	1.14	10.96	1.25	18.44	1.78

All inception models underpredict the number concentration of small particles ($d_m < 6$ nm) at $\phi=1.9$. The discrepancy decreases for $\phi=2$ and the model predictions align well with the measurements. The number concentration of the smallest measured particle (≈ 2 nm) is less affected by equivalence ratio compared to the numerical results. This suggests a stronger sensitivity of the PAH production rate to variation of ϕ from 1.9 to 2.1, which directly impacts soot inception flux. The strong similarity of profiles of acenaphthylene (A2R5) mole fraction and soot inception along the reactor shown in Figure 24 highlights the dominant role of PAH chemistry on soot inception. Another important observation is that A2R5 mole fraction is not affected by the employed inception model. One order of magnitude increase in peak A2R5 mole fraction due to the change of ϕ from 1.9 to 2.1 is amplified leading to two orders of magnitude increase in inception flux.

As shown in Figure 25, d_p along the flow reactor is nearly the same for all inception models at $\phi=1.9$, but the difference becomes noticeable for higher ϕ values. Reactive Dimerization predicts the largest final d_p because it directs more PAH mass to surface growth rather than inception, which is consistent with lower peak number concentration observed in Figure 23. d_p rapidly decreases at the beginning of the reactor flow due to the rise in the production of incipient particles (spherical particles with diameter of 2 nm) that lowers the mean d_p of particles. Then, d_p increases by surface growth towards the end of reactor. The final d_p slightly increases with ϕ , but its range is similar for ϕ values. As shown in Figure 26, soot volume fraction however is very sensitive to ϕ , which can be

explained by the strong effect of ϕ on PAH production, inception flux, and number of particles. The analysis of surface growth rates at end of PFR revealed that more than 95% of soot mass is gained through HACA. Figure 27 illustrates the coupling between N_{agg} and HACA growth rate and their change due to ϕ .

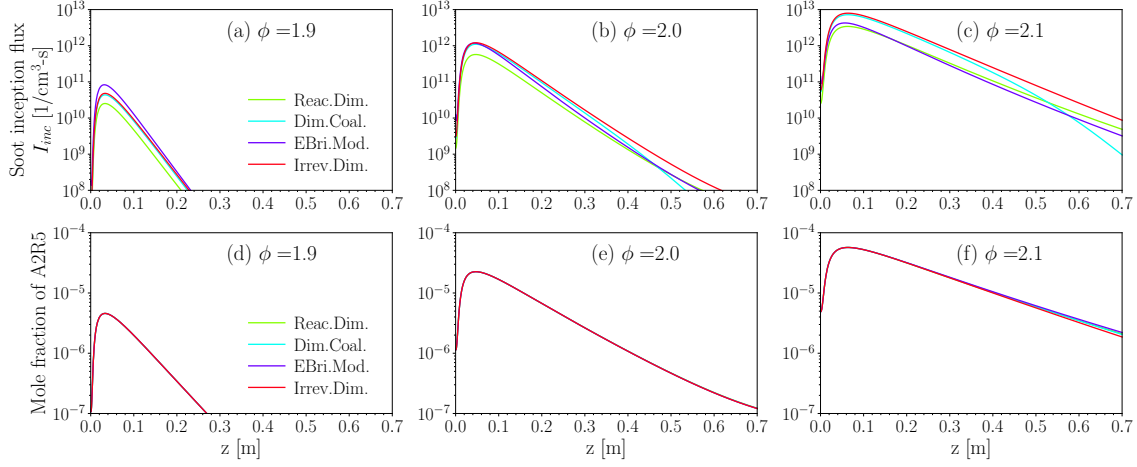


Figure 24: The soot inception flux, I_{inc} and acenaphthylene (A2R5) mole fraction along the PFR for $\phi = 1.9$ (a,d), 2.0 (b,e), and 2.1 (c,f) obtained using KAUST mechanism and different inception models calibrated to match the predictions with measurement [126].

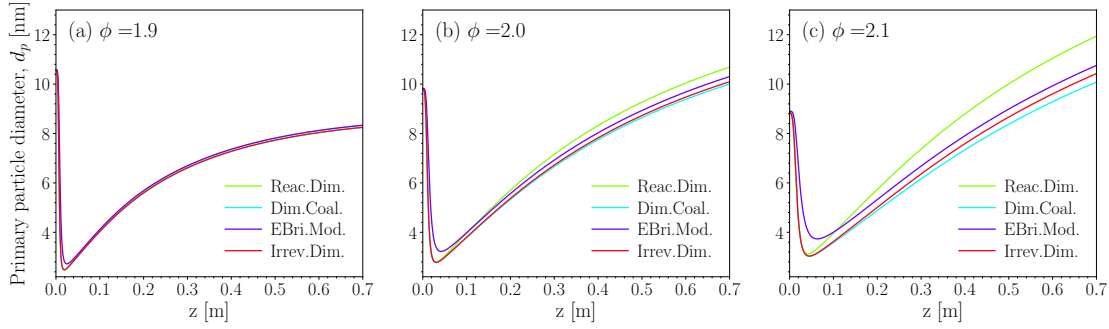


Figure 25: The primary particle diameter, d_p , along the PFR for $\phi = 1.9$ (a), 2.0 (b), and 2.1 (c) obtained using KAUST mechanism and different inception models calibrated to match the predictions with measurement [126].

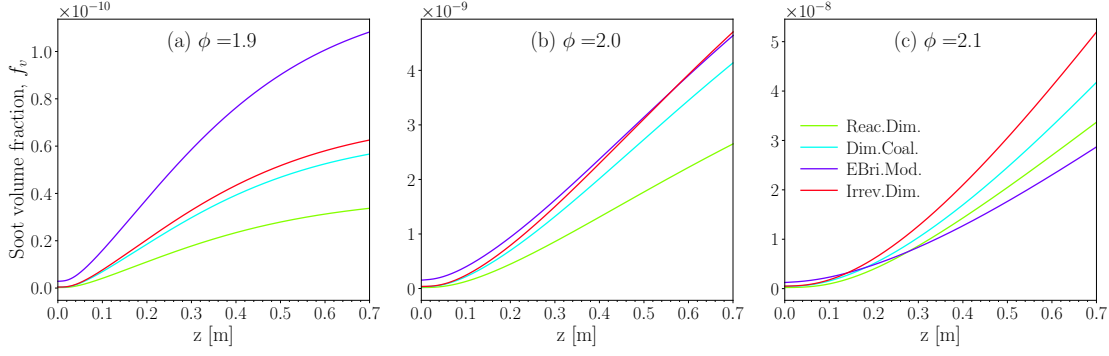


Figure 26: The soot volume fraction, f_v , along the PFR for $\phi = 1.9$ (a), 2.0 (b), and 2.1 (c) obtained using KAUST mechanism and different inception models calibrated to match the predictions with measurement [126].

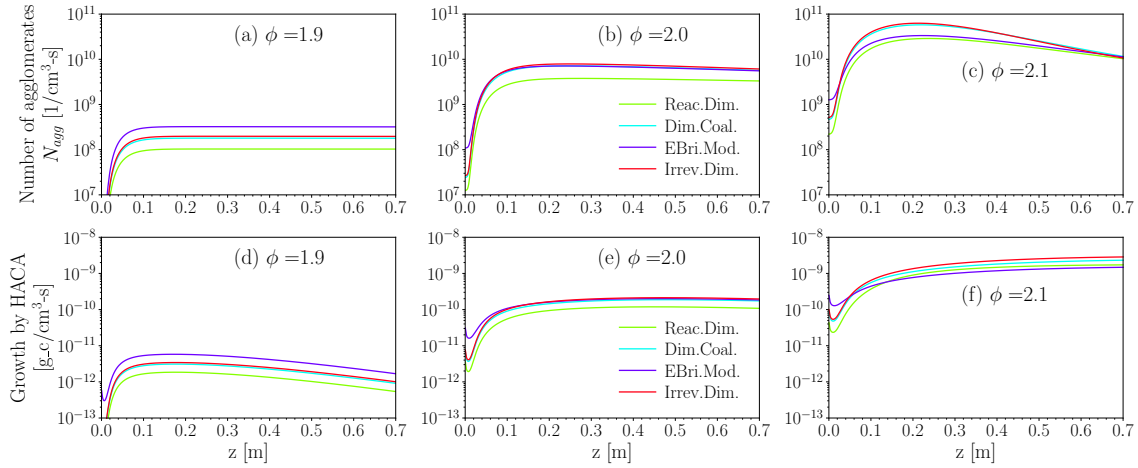


Figure 27: The number of agglomerates, N_{agg} , and the rate of carbon addition by HACA along the PFR for $\phi = 1.9$ (a,d), 2.0 (b,e), and 2.1 (c,f) obtained using KAUST mechanism and different inception models calibrated to match the predictions with measurement [126].

5 Conclusion

This work presents omnisoot as a robust computational tool built on Cantera to simulate soot formation coupled with gas-phase chemistry across various combustion and pyrolysis scenarios. Omnisoot integrates four reactor models, two aerosol dynamics models, and four inception and surface growth models, providing a comprehensive platform for analyzing uncertainties in predicting soot yield and morphology originating from chemical kinetics, inception processes, and surface growth rates. The tool was employed to elucidate differences among inception models in shock tubes, flow reactors, and perfectly stirred reactors.

Global adjustment factors were applied to inception and surface growth rates to accurately reproduce experimental data for each target scenario across a range of parameters, including temperature, pressure, composition, and flow rates. The performance of inception models was evaluated based on soot yield, morphology, size distribution, inception and surface growth rates, and carbon mass source analysis. Although different inception models predicted similar carbon yields that closely matched

experimental observations, they produced varying morphological characteristics. This highlights the importance of characterizing soot morphology to better constrain inception flux and surface growth rate predictions.

Simulations of ethylene pyrolysis in a flow reactor demonstrated the temperature sensitivity of inception models. Irreversible models (Irreversible Dimerization and Dimer Coalescence) effectively captured the bimodal PSD resulting from high inception flux in the lower-temperature region near the reactor exit. However, the Reactive Dimerization and E-Bridge models generated nearly unimodal distributions due to their strong temperature dependence, causing a significant drop in inception flux in the same region.

The PSD sampled at the outlet of a flow reactor downstream of a perfectly stirred reactor showed good agreement with experimental measurements across three equivalence ratios. Simulations indicated that active inception and surface growth primarily occur at high temperatures within the perfectly stirred reactor and at the entrance region of the flow reactor, far upstream of the sampling location. Under these conditions, the particle size distribution, morphology, and inception flux predictions were largely consistent across all inception models, although notable differences were observed in soot volume fraction due to variations in predicted HACA growth rate.

6 Acknowledgements

The research leading to these results has received funding from the Canada Research Chair Program (Grant #CRC-2019-232527) and the Natural Sciences and Engineering Research Council of Canada (Discovery Grant #RGPIN-2019-06330 and -Early Career Supplemental Award #DGECR-2019-00220 and Alliance #576739-2022), Monolith Materials and MITACS (IT28731).

References

- [1] Andrea D’Anna. Combustion-formed nanoparticles. *Proceedings of the Combustion Institute*, 32(1):593–613, 2009.
- [2] Gunnar Myhre, Drew Shindell, and Julia Pongratz. Anthropogenic and natural radiative forcing. 2014.
- [3] Paul JA Borm, Roel PF Schins, and Catrin Albrecht. Inhaled particles and lung cancer, part b: paradigms and risk assessment. *International journal of cancer*, 110(1):3–14, 2004.
- [4] Fabian Rosner, Trisha Bhagde, Daniel S Slaughter, Vassilia Zorba, and Jennifer Stokes-Draut. Techno-economic and carbon dioxide emission assessment of carbon black production. *Journal of Cleaner Production*, 436:140224, 2024.
- [5] International Carbon Black Association et al. Carbon black user’s guide. *available at www.carbon-black.org*, 2016.
- [6] Verónica Palomares, Aintzane Goñi, Izaskun Gil De Muro, Iratxe De Meatza, Miguel Bengoechea, Igor Cantero, and Teófilo Rojo. Conductive additive content balance in li-ion battery cathodes: Commercial carbon blacks vs. in situ carbon from lifepo4/c composites. *J. Power Sources*, 195:7661–7668, 2010. ISSN 0378-7753.
- [7] Mario Commодо, Katharina Kaiser, Gianluigi De Falco, Patrizia Minutolo, Fabian Schulz, Andrea D’Anna, and Leo Gross. On the early stages of soot formation: Molecular structure elucidation by high-resolution atomic force microscopy. *Combustion and Flame*, 205:154–164, 2019.
- [8] Fabian Schulz, Mario Commодо, Katharina Kaiser, Gianluigi De Falco, Patrizia Minutolo, Gerhard Meyer, Andrea D’Anna, and Leo Gross. Insights into incipient soot formation by atomic force microscopy. *Proceedings of the Combustion Institute*, 37(1):885–892, 2019.
- [9] Marina Schenk, Sydnie Lieb, Henning Vieker, André Beyer, Armin Götzhäuser, Hai Wang, and Katharina Kohse-Höinghaus. Imaging nanocarbon materials: soot particles in flames are not structurally homogeneous. *ChemPhysChem*, 14(14):3248–3254, 2013.
- [10] M Reza Kholghy and Valentina G DeRosa. Morphology, composition and optical properties of jet engine-like soot made by a spray flame. *Combustion and Flame*, 231:111480, 2021.
- [11] KO Johansson, F El Gabaly, PE Schrader, MF Campbell, and HA Michelsen. Evolution of maturity levels of the particle surface and bulk during soot growth and oxidation in a flame. *Aerosol Science and Technology*, 51(12):1333–1344, 2017.
- [12] Enoch Dames, Vandad Rohani, and Laurent Fulcheri. Plasma chemistry and plasma reactors for turquoise hydrogen and carbon nanomaterials production. In *Advances in Chemical Engineering*, volume 61, pages 253–317. Elsevier, 2023.
- [13] Tianyang Li, Christophe Rehmet, Yan Cheng, Yong Jin, and Yi Cheng. Experimental comparison of methane pyrolysis in thermal plasma. *Plasma Chemistry and Plasma Processing*, 37:1033–1049, 2017.
- [14] Laurent Fulcheri, Vandad-Julien Rohani, Elliott Wyse, Ned Hardman, and Enoch Dames. An energy-efficient plasma methane pyrolysis process for high yields of carbon black and hydrogen. *International Journal of Hydrogen Energy*, 48(8):2920–2928, 2023.
- [15] Shashank Reddy Patlolla, Kyle Katsu, Amir Sharafian, Kevin Wei, Omar E Herrera, and Walter Mérida. A review of methane pyrolysis technologies for hydrogen production. *Renewable and Sustainable Energy Reviews*, 181:113323, 2023.

- [16] Ann Y Watson and Peter A Valberg. Carbon black and soot: two different substances. *AIHAJ-American Industrial Hygiene Association*, 62(2):218–228, 2001.
- [17] C Russo, A Tregrossi, and A Ciajolo. Dehydrogenation and growth of soot in premixed flames. *Proceedings of the Combustion Institute*, 35(2):1803–1809, 2015.
- [18] Madhu Singh and Randy L Vander Wal. Nanostructure quantification of carbon blacks. *C*, 5(1):2, 2018.
- [19] Randy L Vander Wal, Aleksey Yezerets, Neal W Currier, Do Heui Kim, and Chong Min Wang. Hrtem study of diesel soot collected from diesel particulate filters. *Carbon*, 45(1):70–77, 2007.
- [20] Magín Lapuerta, Javier Barba, Anton D Sediako, Mohammad Reza Kholghy, and Murray J Thomson. Morphological analysis of soot agglomerates from biodiesel surrogates in a coflow burner. *Journal of Aerosol Science*, 111:65–74, 2017.
- [21] Hai Wang. Formation of nascent soot and other condensed-phase materials in flames. *Proc Combust Inst.*, 33:41–67, 2011. ISSN 15407489.
- [22] Michael Frenklach and Hai Wang. Detailed modeling of soot particle nucleation and growth. In *Symposium (International) on Combustion*, volume 23, pages 1559–1566. Elsevier, 1991.
- [23] Steffen Salenbauch, Alberto Cuoci, Alessio Frassoldati, Chiara Saggese, Tiziano Faravelli, and Christian Hasse. Modeling soot formation in premixed flames using an extended conditional quadrature method of moments. *Combustion and Flame*, 162(6):2529–2543, 2015.
- [24] Pascale Desgroux, Alessandro Faccinetto, Xavier Mercier, Thomas Mouton, Damien Aubagnac Karkar, and Abderrahman El Bakali. Comparative study of the soot formation process in a “nucleation” and a “sooting” low pressure premixed methane flame. *Combustion and Flame*, 184:153–166, 2017.
- [25] Yu Wang, Abhijeet Raj, and Suk Ho Chung. Soot modeling of counterflow diffusion flames of ethylene-based binary mixture fuels. *Combustion and Flame*, 162(3):586–596, 2015.
- [26] Lei Xu, Fuwu Yan, Mengxiang Zhou, and Yu Wang. An experimental and modeling study on sooting characteristics of laminar counterflow diffusion flames with partial premixing. *Energy*, 218:119479, 2021.
- [27] Mohammad Reza Kholghy, Armin Veshkini, and Murray John Thomson. The core-shell internal nanostructure of soot—a criterion to model soot maturity. *Carbon*, 100:508–536, 2016.
- [28] Armin Veshkini, Seth B Dworkin, and Murray J Thomson. Understanding soot particle size evolution in laminar ethylene/air diffusion flames using novel soot coalescence models. *Combustion Theory and Modelling*, 20(4):707–734, 2016.
- [29] J Houston Miller, Kermit C Smyth, and W Gary Mallard. Calculations of the dimerization of aromatic hydrocarbons: Implications for soot formation. In *Symposium (International) on Combustion*, volume 20, pages 1139–1147. Elsevier, 1985.
- [30] Hassan Sabbah, Ludovic Biennier, Stephen J Klippenstein, Ian R Sims, and Bertrand R Rowe. Exploring the role of pahs in the formation of soot: Pyrene dimerization. *The Journal of Physical Chemistry Letters*, 1(19):2962–2967, 2010.
- [31] Ali Naseri, M Reza Kholghy, Neil A Juan, and Murray J Thomson. Simulating yield and morphology of carbonaceous nanoparticles during fuel pyrolysis in laminar flow reactors enabled by reactive inception and aromatic adsorption. *Combustion and Flame*, 237:111721, 2022.
- [32] Nazly E Sanchez, Alicia Callejas, Angela Millera, Rafael Bilbao, and Maria U Alzueta. Polycyclic aromatic hydrocarbon (pah) and soot formation in the pyrolysis of acetylene and ethylene: effect of the reaction temperature. *Energy & fuels*, 26(8):4823–4829, 2012.

- [33] Sanghwan Cho, Seunghoon Lee, Wonnam Lee, and Sunho Park. Synthesis of primary-particle-size-tuned soot particles by controlled pyrolysis of hydrocarbon fuels. *Energy & Fuels*, 30(8):6614–6619, 2016.
- [34] Mohammad Reza Kholghy, Nick Anthony Eaves, Armin Veshkini, and Murray John Thomson. The role of reactive pah dimerization in reducing soot nucleation reversibility. *Proceedings of the Combustion Institute*, 37(1):1003–1011, 2019.
- [35] Mohammad R Kholghy, Georgios A Kelesidis, and Sotiris E Pratsinis. Reactive polycyclic aromatic hydrocarbon dimerization drives soot nucleation. *Physical Chemistry Chemical Physics*, 20(16):10926–10938, 2018.
- [36] Michael Frenklach and Alexander M Mebel. On the mechanism of soot nucleation. *Physical Chemistry Chemical Physics*, 22(9):5314–5331, 2020.
- [37] Aamir D Abid, Joaquin Camacho, David A Sheen, and Hai Wang. Quantitative measurement of soot particle size distribution in premixed flames—the burner-stabilized stagnation flame approach. *Combustion and Flame*, 156(10):1862–1870, 2009.
- [38] Jörg Appel, Henning Bockhorn, and Michael Frenklach. Kinetic modeling of soot formation with detailed chemistry and physics: laminar premixed flames of c2 hydrocarbons. *Combustion and flame*, 121(1-2):122–136, 2000.
- [39] Guillaume Blanquart and Heinz Pitsch. A joint volume-surface-hydrogen multi-variate model for soot formation. *Combustion generated fine carbonaceous particles*, pages 437–463, 2009.
- [40] Michael Frenklach. Reaction mechanism of soot formation in flames. *Physical chemistry chemical Physics*, 4(11):2028–2037, 2002.
- [41] IT Woods and BS Haynes. Soot surface growth at active sites. *Combustion and flame*, 85(3-4):523–525, 1991.
- [42] Cameron J Dasch. The decay of soot surface growth reactivity and its importance in total soot formation. *Combustion and flame*, 61(3):219–225, 1985.
- [43] Hope A Michelsen, Meredith B Colket, Per-Erik Bengtsson, Andrea D’anna, Pascale Desgroux, Brian S Haynes, J Houston Miller, Graham J Nathan, Heinz Pitsch, and Hai Wang. A review of terminology used to describe soot formation and evolution under combustion and pyrolytic conditions. *ACS nano*, 14(10):12470–12490, 2020.
- [44] OI Obolensky, VV Semenikhina, AV Solov’Yov, and W Greiner. Interplay of electrostatic and van der waals forces in coronene dimer. *International Journal of Quantum Chemistry*, 107(6):1335–1343, 2007.
- [45] FS Lai, SK Friedlander, J Pich, and GM Hidy. The self-preserving particle size distribution for brownian coagulation in the free-molecule regime. *Journal of Colloid and Interface Science*, 39(2):395–405, 1972.
- [46] Raymond D Mountain, George W Mulholland, and Howard Baum. Simulation of aerosol agglomeration in the free molecular and continuum flow regimes. *Journal of Colloid and Interface Science*, 114(1):67–81, 1986.
- [47] Eirini Goudeli, Maximilian L Eggersdorfer, and Sotiris E Pratsinis. Coagulation of agglomerates consisting of polydisperse primary particles. *Langmuir*, 32:9276–9285, 2016. ISSN 0743-7463.
- [48] Georgios A Kelesidis and Eirini Goudeli. Self-preserving size distribution and collision frequency of flame-made nanoparticles in the transition regime. *Proceedings of the Combustion Institute*, 38(1):1233–1240, 2021.

- [49] Georgios A. Kelesidis, Eirini Goudeli, and Sotiris E. Pratsinis. Flame synthesis of functional nanostructured materials and devices: Surface growth and aggregation. *Proc Combust Inst* ., 36:29–50, 2017. ISSN 15407489.
- [50] Georgios A Kelesidis and Sotiris E Pratsinis. A perspective on gas-phase synthesis of nano-materials: Process design, impact and outlook. *Chemical Engineering Journal*, 421:129884, 2021.
- [51] Georgios A. Kelesidis, Eirini Goudeli, and Sotiris E. Pratsinis. Morphology and mobility diameter of carbonaceous aerosols during agglomeration and surface growth. *Carbon*, 121: 527–535, 9 2017. ISSN 00086223.
- [52] Andrei Kazakov and Michael Frenklach. Dynamic modeling of soot particle coagulation and aggregation: Implementation with the method of moments and application to high-pressure laminar premixed flames. *Combustion and flame*, 114(3-4):484–501, 1998.
- [53] F Einar Kruis, Karl A Kusters, Sotiris E Pratsinis, and Brian Scarlett. A simple model for the evolution of the characteristics of aggregate particles undergoing coagulation and sintering. *Aerosol science and technology*, 19(4):514–526, 1993.
- [54] Patrick T Spicer, Olivier Chaoul, Stavros Tsantilis, and Sotiris E Pratsinis. Titania formation by ticl4 gas phase oxidation, surface growth and coagulation. *J. Aerosol Sci.*, 33:17–34, 2002. ISSN 0021-8502.
- [55] Aamir D Abid, Nicholas Heinz, Erik D Tolmachoff, Denis J Phares, Charles S Campbell, and Hai Wang. On evolution of particle size distribution functions of incipient soot in premixed ethylene–oxygen–argon flames. *Combustion and Flame*, 154(4):775–788, 2008.
- [56] X Ma, CD Zangmeister, and MR Zachariah. Soot oxidation kinetics: a comparison study of two tandem ion-mobility methods. *The Journal of Physical Chemistry C*, 117(20):10723–10729, 2013.
- [57] Joaquin Camacho, Changran Liu, Chen Gu, He Lin, Zhen Huang, Quanxi Tang, Xiaoqing You, Chiara Saggese, Yang Li, Heejung Jung, et al. Mobility size and mass of nascent soot particles in a benchmark premixed ethylene flame. *Combustion and Flame*, 162(10):3810–3822, 2015.
- [58] Arto J Gröhn, Sotiris E Pratsinis, and Karsten Wegner. Fluid-particle dynamics during combustion spray aerosol synthesis of zro2. *Chemical Engineering Journal*, 191:491–502, 2012.
- [59] Sotiris E Pratsinis. Simultaneous nucleation, condensation, and coagulation in aerosol reactors. *Journal of colloid and interface science*, 124(2):416–427, 1988.
- [60] G Blanquart and H Pitsch. Analyzing the effects of temperature on soot formation with a joint volume-surface-hydrogen model. *Combustion and Flame*, 156(8):1614–1626, 2009.
- [61] Michael Frenklach and Stephen J Harris. Aerosol dynamics modeling using the method of moments. *Journal of colloid and interface science*, 118(1):252–261, 1987.
- [62] Stavros Tsantilis and Sotiris E Pratsinis. Soft-and hard-agglomerate aerosols made at high temperatures. *Langmuir*, 20(14):5933–5939, 2004.
- [63] Peter R Lindstedt. Simplified soot nucleation and surface growth steps for non-premixed flames. In *Soot formation in combustion: mechanisms and models*, pages 417–441. Springer, 1994.
- [64] Yun Xiong and Sotiris E Pratsinis. Formation of agglomerate particles by coagulation and sintering—part i. a two-dimensional solution of the population balance equation. *J. Aerosol Sci.*, 24:283–300, 1993. ISSN 0021-8502.

- [65] MA Schiener and RP Lindstedt. Transported probability density function based modelling of soot particle size distributions in non-premixed turbulent jet flames. *Proceedings of the Combustion Institute*, 37(1):1049–1056, 2019.
- [66] Fred Gelbard, Yoram Tambour, and John H Seinfeld. Sectional representations for simulating aerosol dynamics. *Journal of colloid and interface science*, 76(2):541–556, 1980.
- [67] SH Park and SN Rogak. A novel fixed-sectional model for the formation and growth of aerosol agglomerates. *Journal of Aerosol Science*, 35(11):1385–1404, 2004.
- [68] Themis Matsoukas and Sheldon K Friedlander. Dynamics of aerosol agglomerate formation. *Journal of Colloid and Interface Science*, 146(2):495–506, 1991.
- [69] NA Fuchs. The mechanics of aerosol pergamon. *New York*, 1964.
- [70] Yun Xiong and Sotiris E Pratsinis. Formation of agglomerate particles by coagulation and sintering—part i. a two-dimensional solution of the population balance equation. *Journal of Aerosol Science*, 24(3):283–300, 1993.
- [71] Nick A Eaves, Qingan Zhang, Fengshan Liu, Hongsheng Guo, Seth B Dworkin, and Murray J Thomson. Coflame: A refined and validated numerical algorithm for modeling sooting laminar coflow diffusion flames. *Computer Physics Communications*, 207:464–477, 2016.
- [72] Seth B Dworkin, Qingan Zhang, Murray J Thomson, Nadezhda A Slavinskaya, and Uwe Riedel. Application of an enhanced pah growth model to soot formation in a laminar coflow ethylene/air diffusion flame. *Combustion and Flame*, 158(9):1682–1695, 2011.
- [73] Fengshan Liu, Ahmet E Karataş, Ömer L Gülder, and Mingyan Gu. Numerical and experimental study of the influence of co2 and n2 dilution on soot formation in laminar coflow c2h4/air diffusion flames at pressures between 5 and 20 atm. *Combustion and Flame*, 162(5):2231–2247, 2015.
- [74] Andrea Nobili, Warumporn Pejpichestakul, Matteo Pelucchi, Alberto Cuoci, Carlo Cavallotti, and Tiziano Faravelli. Modeling soot particles as stable radicals: a chemical kinetic study on formation and oxidation. part ii. soot oxidation in flow reactors and laminar flames. *Combustion and Flame*, 243:112072, 2022.
- [75] Alberto Cuoci, Alessio Frassoldati, Tiziano Faravelli, and Eliseo Ranzi. Opensmoke++: An object-oriented framework for the numerical modeling of reactive systems with detailed kinetic mechanisms. *Computer Physics Communications*, 192:237–264, 2015.
- [76] Alberto Cuoci, Alessio Frassoldati, Tiziano Faravelli, and Eliseo Ranzi. A computational tool for the detailed kinetic modeling of laminar flames: Application to c2h4/ch4 coflow flames. *Combustion and Flame*, 160(5):870–886, 2013.
- [77] David G. Goodwin, Harry K. Moffat, Ingmar Schoegl, Raymond L. Speth, and Bryan W. Weber. Cantera: An object-oriented software toolkit for chemical kinetics, thermodynamics, and transport processes. <https://www.cantera.org>, 2022. Version 2.6.0.
- [78] Hope A Michelsen. Effects of maturity and temperature on soot density and specific heat. *Proceedings of the Combustion Institute*, 38(1):1197–1205, 2021.
- [79] Kirk A Jensen, Jill M Suo-Anttila, and Linda G Blevins. Measurement of soot morphology, chemistry, and optical properties in the visible and near-infrared spectrum in the flame zone and overfire region of large jp-8 pool fires. *Combustion science and technology*, 179(12):2453–2487, 2007.
- [80] Bonnie J McBride. *Coefficients for calculating thermodynamic and transport properties of individual species*, volume 4513. National Aeronautics and Space Administration, Office of Management . . . , 1993.

- [81] Robert J Kee, Michael E Coltrin, Peter Glarborg, and Huayang Zhu. *Chemically reacting flow: theory, modeling, and simulation*. John Wiley & Sons, 2017.
- [82] Skjalg E Haaland. Simple and explicit formulas for the friction factor in turbulent pipe flow. 1983.
- [83] FP Berger and K-FF-L Hau. Mass transfer in turbulent pipe flow measured by the electrochemical method. *International Journal of Heat and Mass Transfer*, 20(11):1185–1194, 1977.
- [84] George W Mulholland, RJ Samson, RD Mountain, and MH Ernst. Cluster size distribution for free molecular agglomeration. *Energy & Fuels*, 2(4):481–486, 1988.
- [85] Georgios A Kelesidis and Sotiris E Pratsinis. Estimating the internal and surface oxidation of soot agglomerates. *Combustion and Flame*, 209:493–499, 2019.
- [86] Jérôme Yon, A Bescond, and F-X Ouf. A simple semi-empirical model for effective density measurements of fractal aggregates. *Journal of Aerosol Science*, 87:28–37, 2015.
- [87] Jenny Rissler, Maria E Messing, Azhar I Malik, Patrik T Nilsson, Erik Z Nordin, Mats Bohgard, Mehri Sanati, and Joakim H Pagels. Effective density characterization of soot agglomerates from various sources and comparison to aggregation theory. *Aerosol Science and Technology*, 47(7):792–805, 2013.
- [88] Ganesan Narsimhan and Eli Ruckenstein. The brownian coagulation of aerosols over the entire range of knudsen numbers: Connection between the sticking probability and the interaction forces. *Journal of colloid and interface science*, 104(2):344–369, 1985.
- [89] Antonio D’Alessio, AC Barone, R Cau, Andrea D’Anna, and P Minutolo. Surface deposition and coagulation efficiency of combustion generated nanoparticles in the size range from 1 to 10 nm. *Proceedings of the Combustion Institute*, 30(2):2595–2603, 2005.
- [90] Hwa-Chi Wang and Gerhard Kasper. Filtration efficiency of nanometer-size aerosol particles. *Journal of Aerosol Science*, 22(1):31–41, 1991.
- [91] Dingyu Hou, Diyu Zong, Casper S Lindberg, Markus Kraft, and Xiaoqing You. On the coagulation efficiency of carbonaceous nanoparticles. *Journal of Aerosol Science*, 140:105478, 2020.
- [92] Anna Ciajolo, Rosalba Barbella, Antonio Tregrossi, and Loretta Bonfanti. Spectroscopic and compositional signatures of pah-loaded mixtures in the soot inception region of a premixed ethylene flame. In *Symposium (International) on Combustion*, volume 27, pages 1481–1487. Elsevier, 1998.
- [93] Christopher Betrancourt, Fengshan Liu, Pascale Desgroux, Xavier Mercier, Alessandro Facinnetto, Maurin Salamanca, Lena Ruwe, Katharina Kohse-Höinghaus, Daniel Emmrich, André Beyer, et al. Investigation of the size of the incandescent incipient soot particles in premixed sooting and nucleation flames of n-butane using lii, him, and 1 nm-smgs. *Aerosol Science and Technology*, 51(8):916–935, 2017.
- [94] Hope A Michelsen. Probing soot formation, chemical and physical evolution, and oxidation: A review of in situ diagnostic techniques and needs. *Proceedings of the Combustion Institute*, 36(1):717–735, 2017.
- [95] Nikolaj A Fuchs, RE Daisley, Marina Fuchs, CN Davies, and ME Straumanis. The mechanics of aerosols, 1965.
- [96] Jin Jwang Wu and Richard C Flagan. A discrete-sectional solution to the aerosol dynamic equation. *Journal of Colloid and interface Science*, 123(2):339–352, 1988.

- [97] SH Park, SN Rogak, WK Bushe, JZ Wen, and MJ Thomson. An aerosol model to predict size and structure of soot particles. *Combustion Theory and Modelling*, 9(3):499–513, 2005.
- [98] Michael Frenklach. New form for reduced modeling of soot oxidation: Accounting for multi-site kinetics and surface reactivity. *Combustion and Flame*, 201:148–159, 2019.
- [99] BS Haynes and H Gg Wagner. The surface growth phenomenon in soot formation. *Zeitschrift für Physikalische Chemie*, 133(2):201–213, 1982.
- [100] Stephen J Harris and Anita M Weiner. Chemical kinetics of soot particle growth. *Annual Review of Physical Chemistry*, 36(1):31–52, 1985.
- [101] KH Homann. Formation of large molecules, particulates and ions in premixed hydrocarbon flames; progress and unresolved questions. In *Symposium (International) on Combustion*, volume 20, pages 857–870. Elsevier, 1985.
- [102] Armin Veshkini. *Understanding Soot Particle Growth Chemistry and Particle Sizing Using a Novel Soot Growth and Formation Model*. University of Toronto (Canada), 2015.
- [103] Bin Zhao, Zhiwei Yang, Murray V Johnston, Hai Wang, Anthony S Wexler, Michael Balthasar, and Markus Kraft. Measurement and numerical simulation of soot particle size distribution functions in a laminar premixed ethylene-oxygen-argon flame. *Combustion and Flame*, 133(1-2):173–188, 2003.
- [104] Joachim Happold, Horst-Henning Grotheer, and Manfred Aigner. Soot precursors consisting of stacked pericondensed pahs. *Combustion generated fine carbonaceous particles*, pages 275–285, 2009.
- [105] K Olof Johansson, Tyler Dillstrom, Matteo Monti, Farid El Gabaly, Matthew F Campbell, Paul E Schrader, Denisia M Popolan-Vaida, Nicole K Richards-Henderson, Kevin R Wilson, Angela Violi, et al. Formation and emission of large furans and oxygenated hydrocarbons from flames. *Proceedings of the National Academy of Sciences*, 113(30):8374–8379, 2016.
- [106] J Houston Miller, W Gary Mallard, and Kermit C Smyth. Intermolecular potential calculations for polycyclic aromatic hydrocarbons. *The Journal of Physical Chemistry*, 88(21):4963–4970, 1984.
- [107] J Houston Miller. The kinetics of polynuclear aromatic hydrocarbon agglomeration in flames. In *Symposium (International) on Combustion*, volume 23, pages 91–98. Elsevier, 1991.
- [108] Yoichiro Araki, Yoshiya Matsukawa, Yasuhiro Saito, Yohsuke Matsushita, Hideyuki Aoki, Koki Era, and Takayuki Aoki. Effects of carrier gas on the properties of soot produced by ethylene pyrolysis. *Fuel Processing Technology*, 213:106673, 2021.
- [109] Binxuan Sun, Stelios Rigopoulos, and Anxiong Liu. Modelling of soot coalescence and aggregation with a two-population balance equation model and a conservative finite volume method. *Combustion and Flame*, 229:111382, 2021.
- [110] A Tregrossi, A Ciajolo, and R Barbella. The combustion of benzene in rich premixed flames at atmospheric pressure. *Combustion and flame*, 117(3):553–561, 1999.
- [111] M Reza Kholghy and Georgios A Kelesidis. Surface growth, coagulation and oxidation of soot by a monodisperse population balance model. *Combustion and Flame*, 227:456–463, 2021.
- [112] Srinivas Vemury and Sotiris E Pratsinis. Self-preserving size distributions of agglomerates. *Journal of Aerosol Science*, 26(2):175–185, 1995.
- [113] Eirini Goudeli, Maximilian L Eggersdorfer, and Sotiris E Pratsinis. Coagulation–agglomeration of fractal-like particles: Structure and self-preserving size distribution. *Langmuir*, 31(4):1320–1327, 2015.

- [114] Yiqing Wang, Wang Han, Thorsten Zirwes, Antonio Attili, Liming Cai, Henning Bockhorn, Lijun Yang, and Zheng Chen. A systematic analysis of chemical mechanisms for ethylene oxidation and pah formation. *Combustion and Flame*, 253:112784, 2023.
- [115] G Blanquart, P Pepiot-Desjardins, and H Pitsch. Chemical mechanism for high temperature combustion of engine relevant fuels with emphasis on soot precursors. *Combustion and Flame*, 156(3):588–607, 2009.
- [116] Yu Wang, Abhijeet Raj, and Suk Ho Chung. A pah growth mechanism and synergistic effect on pah formation in counterflow diffusion flames. *Combustion and flame*, 160(9):1667–1676, 2013.
- [117] Chiara Saggese, Sara Ferrario, Joaquin Camacho, Alberto Cuoci, Alessio Frassoldati, Eliseo Ranzi, Hai Wang, and Tiziano Faravelli. Kinetic modeling of particle size distribution of soot in a premixed burner-stabilized stagnation ethylene flame. *Combustion and Flame*, 162(9):3356–3369, 2015.
- [118] Maximilian Hellmuth, Raymond Langer, Anita Meraviglia, Joachim Beeckmann, and Heinz Pitsch. The role of c3 and c4 species in forming naphthalene in counterflow diffusion flames. *Proceedings of the Combustion Institute*, 40(1-4):105620, 2024.
- [119] Long Zhu, Snehasish Panigrahy, Sarah N Elliott, Stephen J Klippenstein, Mohammadreza Baigmohammadi, A Abd El-Sabor Mohamed, Joshua W Hargis, Sulaiman Alturaifi, Olivier Mathieu, Eric L Petersen, et al. A wide range experimental study and further development of a kinetic model describing propane oxidation. *Combustion and Flame*, 248:112562, 2023.
- [120] Yue Zhang, Wendi Dong, Laurien Vandewalle, Rui Xu, Gregory Smith, and Hai Wang. Foundational Fuel Chemistry Model Version 2.0 (FFCM-2), 2023. URL <https://web.stanford.edu/group/haiwanglab/FFCM2>.
- [121] Jacob W Martin, Dingyu Hou, Angiras Menon, Laura Pascasio, Jethro Akroyd, Xiaoqing You, and Markus Kraft. Reactivity of polycyclic aromatic hydrocarbon soot precursors: implications of localized π -radicals on rim-based pentagonal rings. *The Journal of Physical Chemistry C*, 123(43):26673–26682, 2019.
- [122] GL Agafonov, IV Biler, PA Vlasov, IV Zhil'tsova, Yu A Kolbanovskii, VN Smirnov, and AM Tereza. Unified kinetic model of soot formation in the pyrolysis and oxidation of aliphatic and aromatic hydrocarbons in shock waves. *Kinetics and Catalysis*, 57:557–572, 2016.
- [123] SC Lee and CL Tien. Optical constants of soot in hydrocarbon flames. In *Symposium (international) on combustion*, volume 18, pages 1159–1166. Elsevier, 1981.
- [124] GL Agafonov, PA Vlasov, and VN Smirnov. Soot formation in the pyrolysis of benzene, methylbenzene, and ethylbenzene in shock waves. *Kinetics and Catalysis*, 52:358–370, 2011.
- [125] Junyu Mei, Mengda Wang, Xiaoqing You, and Chung K Law. Quantitative measurement of particle size distributions of carbonaceous nanoparticles during ethylene pyrolysis in a laminar flow reactor. *Combustion and Flame*, 200:15–22, 2019.
- [126] Samuel L Manzello, David B Lenhert, Ahmet Yozgatligil, Michael T Donovan, George W Mulholland, Michael R Zachariah, and Wing Tsang. Soot particle size distributions in a well-stirred reactor/plug flow reactor. *Proceedings of the Combustion Institute*, 31(1):675–683, 2007.
- [127] David B Lenhert and Samuel L Manzello. Effects of benzene and naphthalene addition on soot inception in a well-stirred reactor/plug flow reactor. *Proceedings of the Combustion Institute*, 32(1):657–664, 2009.
- [128] Scott Stouffer, Richard Striebig, Joseph Zelina, and Charles Frayne. Combustion particulates mitigation investigation using a well-stirred reactor. In *38th AIAA/ASME/SAE/ASEE Joint Propulsion Conference & Exhibit*, page 3723, 2002.

Supplementary Material

Omnisoot: an object-oriented computational package for the simulation of the gas phase synthesis of Carbon Black

Mohammad Adib^{1,*}, Sina Kazemi¹, M. Reza Kholgy^{1,*}

*Corresponding author

¹ Department of Mechanical and Aerospace Engineering, Carleton University, 1125 Colonel By Dr, Ottawa, ON K1S 5B6, Canada

S1 Gas scrubbing rates

The rate of production/destruction of species involved in soot formation must be taken into account to preserve the mass and energy balance in reactive systems. In order to do that, the production rate of gaseous species calculated by Cantera must be corrected for the rate of release/consumption due to PAH growth and surface reaction models calculated in the previous sections.

$$\left(\frac{d[\text{PAH}_j]}{dt}\right)_{tot} = \left(\frac{d[\text{PAH}_j]}{dt}\right)_{gas} + \left(\frac{d[\text{PAH}_j]}{dt}\right)_{inc} + \left(\frac{d[\text{PAH}_j]}{dt}\right)_{ads}. \quad (\text{S1})$$

H₂ is released to the gas mixture due to inception, PAH adsorption as well as oxidation.

$$\left(\frac{d[\text{H}_2]}{dt}\right)_{tot} = \left(\frac{d[\text{H}_2]}{dt}\right)_{gas} + \left(\frac{d[\text{H}_2]}{dt}\right)_{inc} + \left(\frac{d[\text{H}_2]}{dt}\right)_{ads} + \left(\frac{d[\text{H}_2]}{dt}\right)_{ox}. \quad (\text{S2})$$

Surface growth consumes C₂H₂ and adds H₂ to the gas mixture.

$$\left(\frac{d[\text{C}_2\text{H}_2]}{dt}\right)_{tot} = \left(\frac{d[\text{C}_2\text{H}_2]}{dt}\right)_{gas} + \left(\frac{d[\text{C}_2\text{H}_2]}{dt}\right)_{gr}. \quad (\text{S3})$$

$$\left(\frac{d[\text{H}]}{dt}\right)_{tot} = \left(\frac{d[\text{H}]}{dt}\right)_{gas} + \left(\frac{d[\text{H}]}{dt}\right)_{gr}. \quad (\text{S4})$$

Oxidation uses O₂ and OH to remove carbon from soot particles and generates H₂ and CO.

$$\left(\frac{d[\text{CO}]}{dt}\right)_{tot} = \left(\frac{d[\text{CO}]}{dt}\right)_{gas} + \left(\frac{d[\text{CO}]}{dt}\right)_{ox}. \quad (\text{S5})$$

$$\left(\frac{d[\text{O}_2]}{dt}\right)_{tot} = \left(\frac{d[\text{O}_2]}{dt}\right)_{gas} + \left(\frac{d[\text{O}_2]}{dt}\right)_{ox}. \quad (\text{S6})$$

$$\left(\frac{d[\text{OH}]}{dt}\right)_{tot} = \left(\frac{d[\text{OH}]}{dt}\right)_{gas} + \left(\frac{d[\text{OH}]}{dt}\right)_{ox}. \quad (\text{S7})$$

S2 The Effect of Formation and Sensible Energy of Soot

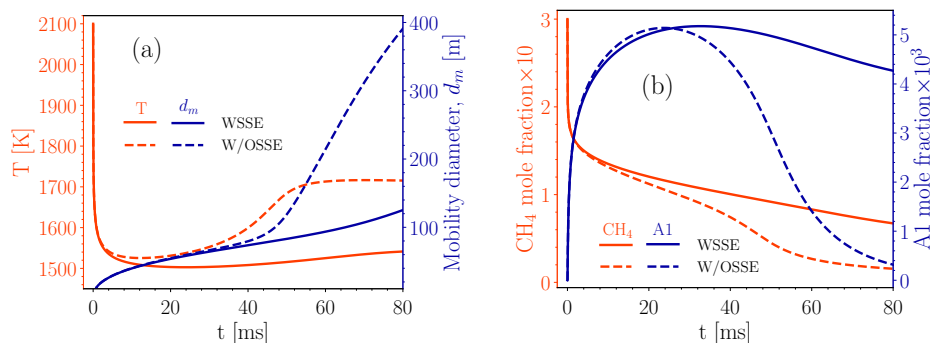


Figure S1: The comparison of temperature and soot mobility diameter, d_m (a) and the mole fraction of methane, CH_4 , and benzene, A1 in the simulation of the pyrolysis of 30% CH_4 -Ar when soot sensible energy is considered (labeled as “WSSE”) and neglected (labeled as “W/OSSE”). The constant volume reactor is used along with Caltech mechanism [115], Reactive Dimerization and the monodisperse population balance model

S3 Validation of Mass and Energy Balance

S3.0.1 Constant Volume Reactor

The pyrolysis of 30% CH_4 diluted in N_2 with the initial temperature and pressure of 2455 K and 3.47 atm, respectively, was simulated using CVR model for the residence time of 40 ms. The combination of available PAH growth and particle dynamics models leads to eight different cases that were simulated to ensure the conservation of mass and energy. Here, we focus on the total elemental balance of carbon and hydrogen because they are involved in soot processes. Figure S2 demonstrates the relative error of total carbon, hydrogen and energy of system for different PAH growth and particle dynamics models in the constant pressure reactor that is less than 10^{-10} for all parameters confirming the validity of model in satisfying the mass and energy balance.

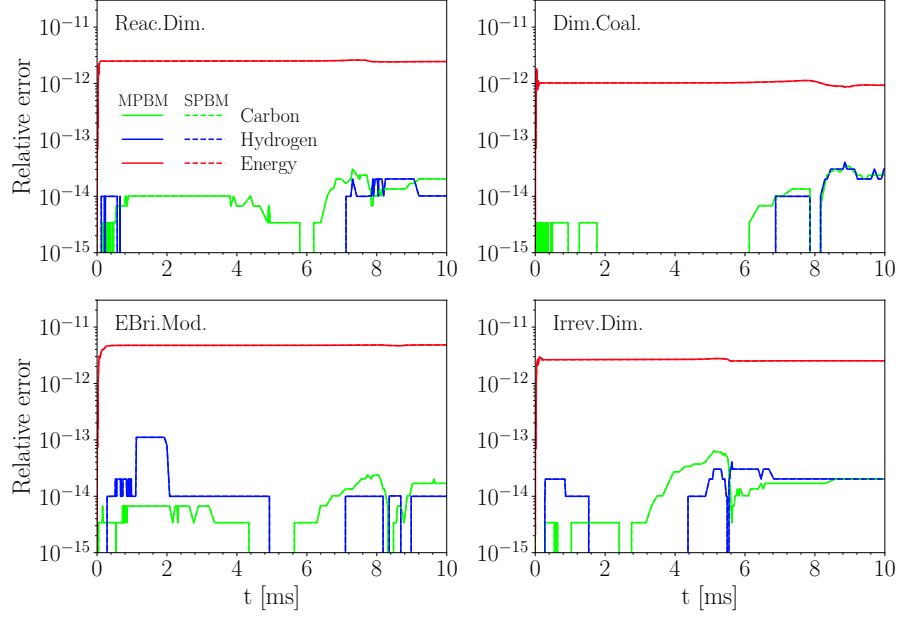


Figure S2: The relative error (residual) of total carbon (red line) and hydrogen (green line) mass, and total internal energy residual of gas and soot (blue line) plotted against residence time during pyrolysis of 30% $\text{CH}_4\text{-N}_2$ at 2455 K and 3.47 atm in CVR simulated using different PAH growth models along with MPBM (solid line) and SPBM (dashed line).

S3.1 Constant Pressure Reactor

The pyrolysis of 5% $\text{CH}_4\text{-Ar}$ in a shock-tube with post-reflected-shock temperature and pressure of $T_5 = 2355$ K and $P_5 = 4.64$ atm, respectively, was simulated using CPR model. Figure S3 shows the relative error of total carbon, hydrogen and energy of system for different PAH growth and particle dynamics models in the constant volume that falls below 10^{-10} for all parameters confirming the validity of model in satisfying the mass and energy balance in the constant pressure reactor using all models.

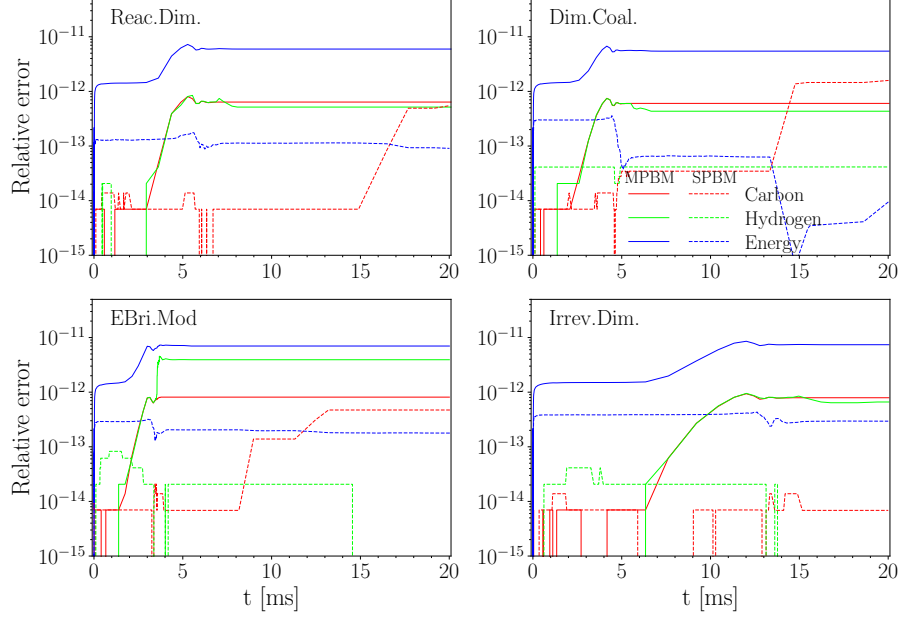


Figure S3: The relative error (residual) of total carbon (red line) and hydrogen (green line) mass, and total internal energy residual of gas and soot (blue line) plotted against residence time during pyrolysis of 5% CH_4 -Ar at 2355 K and 4.64 atm simulated using CPR with different combinations of PAH growth models and particle dynamics models: MPBM (solid line) and SPBM (dashed line).

S3.2 Perfectly Stirred Reactor

The mass and energy balance are investigated for soot formation during ethylene-air oxidation at equivalence ratio, $\phi = 2$ in a perfectly stirred reactor. The simulation conditions were chosen based on the combustor implemented and utilized by Stouffer et al. [128]. The reactants initially at 300 K enter a reactor of 250 ml that works under atmospheric pressure. The simulation is initialized from a high temperature (≈ 2000 K) to avoid trivial solution (cold reactant leaving the reactor with no chemical reactions) and to ensure the model captures a sustained combustion. The residence time of products in the reactor is 8.5 ms. Figure S4 shows the relative error of total elemental carbon and hydrogen mass and total enthalpy of gas and soot, which is less than 10^{-6} for all combinations of particle dynamics and PAH growth models.

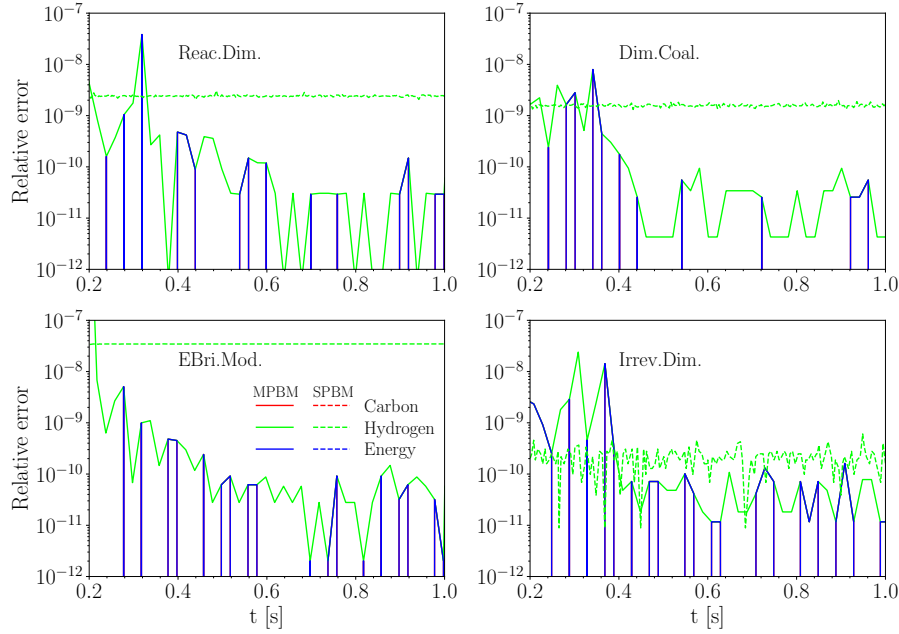


Figure S4: The relative error (residual) of total carbon (red line) and hydrogen (green line) mass, and total internal energy residual of gas and soot (blue line) plotted in simulation time during adiabatic combustion of C_2H_4 -air with $\phi = 2$ at 1 atm simulated using different combinations of PAH growth models and particle dynamics models: MPBM (solid line) and SPBM (dashed line).

S3.3 Plug Flow Reactor

Methane pyrolysis in an adiabatic flow reactor is used to check elemental carbon and hydrogen, and energy balance in the PFR model. The inlet flow enters the reactor at the composition of 30% CH_4 diluted in N_2 , and $T = 2100$ K and $P = 1$ atm. Figure S5 shows the residual of total elemental carbon and hydrogen, and energy up to 40 cm of the reactor length using all PAH growth and particle dynamics models. The residuals are in the order of 10^{-11} and start to grow at the beginning of the reactor by pyrolysis of CH_4 and the formation of intermediate species such as C_2H_2 and PAHs. This initiates soot inception and surface growth affecting the gas chemistry and energy that ends near $z = 10$ cm, and then the coagulation of particles is dominant with no effect on mass and energy of particles. As a result, PFR model of omnisoot satisfies the conservation of the mass and energy.

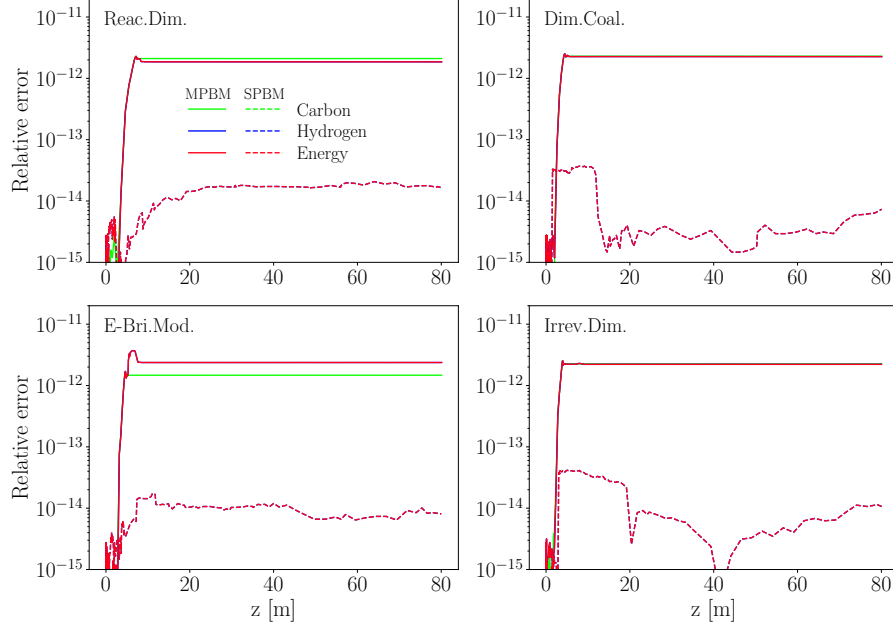


Figure S5: The relative error (residual) of total carbon (red line) and hydrogen (green line) mass, and total internal energy residual of gas and soot (blue line) plotted against reactor length (cm) in the adiabatic flow reactor during pyrolysis of 30% $\text{CH}_4\text{-N}_2$ at 2100 K and 1 atm simulated using different combinations of PAH growth models and particle dynamics models: MPBM (solid line) and SPBM (dashed line).

S4 Validation Collision Frequency

The collision frequency function determines the rate at which two particles collide, which results in the reduction of total number of agglomerates and increase in size. In the absence of strong flow shear or external forces, Brownian motion is the main driving force for particle coagulation. As explained in Sections 2.3.5.1 and 2.3.6.1, omnisooot employs harmonic mean and Fuchs interpolations to calculate collision frequency of agglomerates from free-molecular to continuum regimes based on gas mean free path and particle morphology.

The test case for validation of collision frequency is based on the DEM simulation of 2000 monodisperse spherical particles with the density of 2200 kg/m^3 in a cubic cell with the constant temperature of 298 K and pressure of 1 atm [113]. Figure S6 depicts the collision frequency plotted against Knudsen number ($\text{Kn} = 2\lambda/d_m$) obtained by omnisooot using harmonic mean (red solid line) and Fuchs interpolation (green dashed line) and DEM results of Goudeli et al. [113]. The Fuchs interpretation perfectly matches DEM data over the free-molecular ($\text{Kn} < 10$) to the continuum ($\text{Kn} > 10$) range. Harmonic mean is also in good agreement with the DEM results in the free-molecular and continuum regime, but slightly underpredicts the collision frequency in the transition regime ($0.1 \leq \text{Kn} \leq 10$) with relative errors less than 16%.

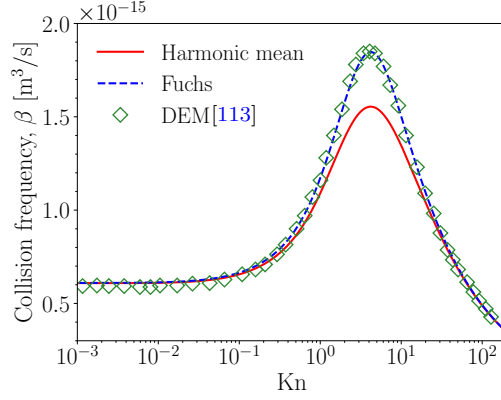


Figure S6: The comparison of collision frequency, β , obtained by omnisooot using harmonic mean (red solid line) and Fuchs interpolation (green dashed line) with DEM results (symbols) [113]

S5 The Effect of Excluding Five-membered Rings

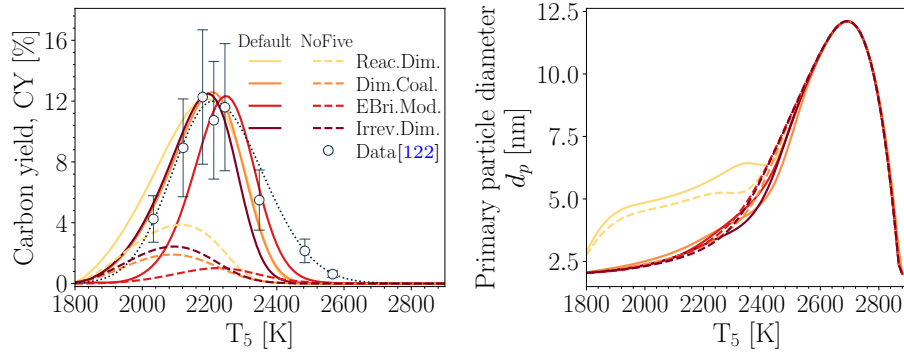


Figure S7: The soot carbon yield, CY, at $t = 1.5$ ms (a) and primary particle diameter, d_p (b) obtained using the default soot precursors listed in Table 1 (denoted by solid line and labeled as “Default”) compared with the same results when five-membered ring PAHs excluded from soot precursors (denoted by dashed line and labeled as “NoFive”). Both cases were obtained using Caltech mechanism and the same equal adjustment factors. The dashed line was added to show the trend in the measurements [122].